



Sodium and Potassium Signatures of Volcanic Satellites Orbiting Close-in Gas Giant Exoplanets

Apurva V. Oza¹ , Robert E. Johnson^{2,3} , Emmanuel Lellouch⁴ , Carl Schmidt⁵ , Nick Schneider⁶ , Chenliang Huang⁷ ,
Diana Gamborino¹ , Andrea Gebek^{1,8} , Aurelien Wytenbach⁹ , Brice-Olivier Demory¹⁰ , Christoph Mordasini¹ ,

Prabal Saxena¹¹, David Dubois¹² , Arielle Moullet¹², and Nicolas Thomas¹

¹Physikalisches Institut, Universität Bern, Bern, Switzerland; apurva.oza@space.unibe.ch

²Engineering Physics, University of Virginia, Charlottesville, VA 22903, USA

³Physics, New York University, 4 Washington Place, New York, NY 10003, USA

⁴LESIA–Observatoire de Paris, CNRS, UPMC Univ. Paris 06, Univ. Denis Diderot, Sorbonne Paris Cite, Meudon, France

⁵Center for Space Physics, Boston University, Boston, MA, USA

⁶Laboratory for Atmospheric and Space Physics, University of Colorado, Boulder, CO, USA

⁷Department of Physics and Astronomy, University of Nevada, Las Vegas, NV, USA

⁸Departement Physik, Eidgenössische Technische Hochschule Zürich, Switzerland

⁹Leiden Observatory, Leiden University, Netherlands

¹⁰Center for Space and Habitability, Universität Bern, Bern, Switzerland

¹¹NASA, Goddard Space Flight Center, Greenbelt, MD, USA

¹²NASA, Ames Research Center, Space Science Division, Moffett Field, CA, USA

Received 2019 January 18; revised 2019 August 20; accepted 2019 August 21; published 2019 November 12

Abstract

Extrasolar satellites are generally too small to be detected by nominal searches. By analogy to the most active body in the solar system, Io, we describe how sodium (Na I) and potassium (K I) gas could be a signature of the geological activity venting from an otherwise hidden exo-Io. Analyzing \sim a dozen close-in gas giants hosting robust alkaline detections, we show that an Io-sized satellite can be stable against orbital decay below a planetary tidal $Q_p \lesssim 10^{11}$. This tidal energy is also focused into the satellite driving an $\sim 10^{5\pm 2}$ higher mass-loss rate than Io's supply to Jupiter's Na exosphere based on simple atmospheric loss estimates. The remarkable consequence is that several exo-Io column densities are, on average, more than sufficient to provide the $\sim 10^{10\pm 1}$ Na cm⁻² required by the equivalent width of exoplanet transmission spectra. Furthermore, the benchmark observations of both Jupiter's extended ($\sim 1000 R_J$) Na exosphere and Jupiter's atmosphere in transmission spectroscopy yield similar Na column densities that are purely exogenic in nature. As a proof of concept, we fit the “high-altitude” Na at WASP-49b with an ionization-limited cloud similar to the observed Na profile about Io. Moving forward, we strongly encourage time-dependent ingress and egress monitoring along with spectroscopic searches for other volcanic volatiles.

Key words: planets and satellites: atmospheres – planets and satellites: composition – planets and satellites: detection – planets and satellites: dynamical evolution and stability – planets and satellites: magnetic fields – planets and satellites: physical evolution

Supporting material: animation

1. Introduction

The 1970s discoveries of sodium (Na I) and potassium (K I) clouds at Io (Brown 1974; Brown & Chaffee 1974; Trafton 1975) turned out to be a revealing observational signature motivating the tidal dissipation theory developed by Peale et al. (1979) that predicted extreme volcanic activity on Io even before *Voyager 1*'s first images of the system (Morabito et al. 1979). This activity was confirmed to be globally extensive by remarkable infrared images by subsequent spacecraft missions, decades of direct-imaging monitoring (e.g., Spencer et al. 2000, 2007; Marchis et al. 2005; de Kleer & de Pater 2016; de Pater et al. 2017; Skrutskie et al. 2017), and, of course, the direct detection of volcanic sulfur species (Lellouch et al. 1990, 1996). The Na and K observations at Io encouraged the search for the venting parent molecules. The subsequent discovery of ionized chlorine in the plasma torus (Küppers & Schneider 2000) suggested the presence of the subsequent direct observations of volcanic salts in the

millimeter/submillimeter, NaCl (Lellouch et al. 2003), and KCl (Moullet et al. 2013). The strong resonance lines in the optical—Na D1 (5895.92 Å), Na D2 (5889.95 Å), K D1 (7698.96 Å), and K D2 (7664.90 Å)—have therefore been pivotal for astronomers characterizing physical processes in atmospheres on solar system bodies, starting from the early observations of Na I in Earth's upper atmosphere in 1967 (Hanson & Donaldson 1967; Hunten 1967; Hunten & Wallace 1967). Thanks to advances in remote and in situ instrumentation, Na I and K I have been detected in silicate (i.e., Io, Mercury, the Moon) and icy (i.e., Europa, comets) bodies but never in H/He envelopes such as the giant planet atmospheres of our solar system. In fact, the origin of Jupiter's Na I exosphere extending to $\sim 1000 R_J$ is Io's volcanism interacting with Jupiter's magnetospheric plasma (e.g., Mendillo et al. 1990; Wilson et al. 2002; Thomas et al. 2004). Table 1 summarizes the spectral observations of the Na and K alkaline metals at several solar system bodies.

Following the first detection of a component of an extrasolar atmosphere, Na I at HD 209458b (Charbonneau et al. 2002), Johnson & Huggins (2006) considered the possible effect of material from an orbiting moon, gas torus, or debris ring on the exoplanet transit spectra. At the time, it was thought that satellite



Original content from this work may be used under the terms of the [Creative Commons Attribution 3.0 licence](https://creativecommons.org/licenses/by/3.0/). Any further distribution of this work must maintain attribution to the author(s) and the title of the work, journal citation and DOI.

Table 1
Alkaline Atmospheres for Silicate and Icy Bodies Measured in situ and Remotely in the Solar System

Body	$N_{\text{Na}} \text{ (cm}^{-2}\text{)}$	Na/K	Origin
^a Comets	$\sim 8 \times 10^{11}$	Na/K = 54 ± 14	Photodesorption/solar wind sputtering
^b Mercury	$\sim 8 \times 10^{11}$	Na/K = 80–190	Photon-stimulated desorption
^c Io	$\sim 5 \times 10^9\text{--}10^{12}$	Na/K = 10 ± 3 NaCl/KCl = 5.75 ± 0.5	Atmospheric sputtering/pickup ions
^d Europa	$\sim 2 \times 10^{10}$	Na/K = 25 ± 2	Surface sputtering, cryovolcanism?
^e Moon	$\sim 5 \times 10^{10}$	Na/K = 6	Photodesorption and meteors
^f Enceladus	$\lesssim 10^9$	Na/K ~ 100	Cryovolcanism
^g Earth*	$\sim 8 \times 10^{11}$	Na/K ~ 100	Micrometeorite ablation
^h Jupiter**	$\sim 7 \times 10^9$	Unknown	Iogenic streams, micrometeorites, impacts
ⁱ Sun	Solar abundance	Na/K $\sim 16 \pm 2$	Protosolar nebula

Notes. For each body, we quote the radial column density for Na I, if observed. The origin of Na I and K I for most bodies is due to space weathering or [cryo] volcanism. We note that Europa and Enceladus likely source Na I from an NaCl-rich water ocean, and therefore Na I could also indicate the presence of water. Direct [cryo]volcanism at both Io and Enceladus is also expected to be NaCl-rich, which subsequently dissociates to Na. The K I observed at Io is thought to be of similar origin to Na I, dissociating from KCl as well. The NaCl/KCl ratio in the atmosphere is a factor of 2 less than the Na/K ratio in the escaping atmosphere, probing the lower and upper atmosphere of Io, respectively. *Earth’s Na I observed in the mesosphere originates from ablation of IDPs. **Jupiter’s upper atmosphere Na I column density is computed in Section 3 of this work. The Na/K for the solar abundance is also tabulated at $\sim 16 \pm 2$.

^a Leblanc et al. (2008); Schmidt et al. (2015b, 2016); Schmidt (2016); Fulle et al. (2013).

^b Sprague et al. (1997); Potter & Morgan (1985, 1986).

^c Burger et al. (2001); Trafton (1975); Thomas (1996); Lellouch et al. (2003); Moullet et al. (2015).

^d Leblanc et al. (2005, 2002); Brown & Hill (1996); Brown (2001).

^e Szalay et al. (2016); Wilson et al. (2006); Potter & Morgan (1988).

^f Postberg et al. (2009); Schneider et al. (2009).

^g Slipher (1929); Hunten (1967); Sullivan & Hunten (1962, 1964); Gardner et al. (2014).

^h Montañés-Rodríguez et al. (2015); this work.

ⁱ Asplund et al. (2009).

orbits around close-in gas giant exoplanets (hot Jupiters) might not be stable; therefore, Johnson & Huggins (2006) suggested that large outgassing clouds of neutrals and/or ions might only be observable for giant exoplanets orbiting at $\gtrsim 0.2$ au. While larger orbital distances are still safer places to search for a satellite, we confirm that close-in gas giant satellites can be more stable than expected. Furthermore, the rapid orbital periods of these close-in satellites enable an efficient transit search. While the above-mentioned Na I exosphere out to $\sim 1000 R_J$ shrinks to $\sim 1 R_J$ due to the far shorter photoionization lifetime of Na I, recent understanding of orbital stability by Cassidy et al. (2009) results in a stabilizing stellar tide well within < 0.2 au driving up to 6 orders of magnitude more heat into the satellite sourcing a density enhancement of $\sim 3\text{--}6$ orders of magnitude into the planetary system. This in turn results in Na I clouds ranging from $\sim 10^{10}$ to $10^{13} \text{ Na cm}^{-2}$ readily discernible by transmission spectroscopy. In fact, a large number of new transmission spectroscopy observations have detected this range of alkaline column densities, which we will evaluate individually in this work. This pursuit was also motivated by the recent evaluation of the uncertainties in the interpretation of the alkaline absorption features at hot Jupiters (Heng et al. 2015; Heng 2016), which has led to the suggestion described here that an exogenic¹³ source from an active satellite might not be unreasonable for certain hot Jupiters. Therefore, we first review recent work describing the range of stable orbits for moons at close-in hot Jupiters. We then analyze a recently published observation of Jupiter showing that the spectral signature of Na I has an external origin. We then describe the mass-loss history and influence of an irradiated, active exomoon at a hot Jupiter, and, finally, we translate these mass-loss rates to column densities, tentatively confirming that

such a signature is consistent with observations at a number of hot Jupiters. Lastly, we provide order-of-magnitude predictions of additional signatures that could more conclusively confirm the first exo-Io.

2. Tidal Stability of an Exo-Io

The dynamic stability of extrasolar satellites depends strongly on the uncertain tidal factor: $Q_{p,s} \propto \dot{E}_{p,s}^{-1}$. Here \dot{E}_p is the energy dissipated by tides into the planetary body (orbital decay) and \dot{E}_s into its orbiting satellite (satellite heating), which is also forced by a third body, the host star. Cassidy et al. (2009) studied both the orbital decay and heating of satellites by considering the circular restricted three-body problem for a satellite, hot Jupiter, and host star. It was shown that if the tidal Q for the planet, Q_p , is of the order of the equilibrium tide limit, $Q_p \sim 10^{12}$, as first derived by Goldreich & Nicholson (1977) and improved by Wu (2005a), even Earth-mass exomoons around hot Jupiters could be tidally stable on $\sim \text{Gyr}$ timescales. Kepler data have not yet detected such exomoons, except for the recent tentative identification of a Uranus-sized candidate, Kepler 1625-b, at ~ 1 au (Teachey & Kipping 2018; Heller et al. 2019; Kreidberg et al. 2019). The observation of a close-in exomoon would, in principle, be able to constrain the low tidal Q values used in the literature (Barnes & O’Brien 2002; Weidner & Horne 2010) previously set to Jupiter’s $\sim 10^5$ (Lainey & Tobie 2005). As shown by Cassidy et al. (2009) and later expanded upon in Sections 4 and 4.2.3, significant mass loss might have substantially eroded large satellites (e.g., Domingos et al. 2006), decreasing their ability to be detected by mass-dependent searches such as transit timing variations (e.g., Agol et al. 2005; Kipping 2009). An exomoon search independent of the satellite size is therefore needed.

¹³ In the following, we refer to processes intrinsic to the gas giant as endogenic and those external, in our case to the satellite or debris ring, as exogenic.

Table 2
Observed Stellar System Parameters

Stellar System	Type	T_*	m_v	M_* (M_\odot)	M_p (M_J)	R_* (R_p)	R_p (R_J)	ρ (g cm^{-3})	t_* (Gyr)	a_p (R_*)	τ_p (days)
WASP-52	K2V	5000	12.0	0.87	0.46	6.06	1.27	0.28	0.4 ± 0.3	7.40	1.75
WASP-76	F7	6250	9.5	1.46	0.92	9.20	1.83	0.19	~ 5	4.10	1.81
HD 189733	K2V	4875	7.66	0.85	1.16	6.88	1.14	0.98	4.3 ± 2.8	8.28	2.22
XO-2 N	K0V	5340	11.18	0.98	0.62	9.64	0.97	0.83	6.3 ± 2.4	8.23	2.62
WASP-49	G6V	5600	11.36	0.72	0.38	9.06	1.11	0.34	~ 5	7.83	2.78
HAT-P-12	K4	4650	12.84	0.73	0.21	7.14	0.95	0.30	2.5 ± 2	11.80	3.21
WASP-6	G8V	5450	12.4	0.89	0.50	6.92	1.22	0.34	11 ± 7	10.41	3.36
WASP-31	F	5540	11.7	1.16	0.48	7.85	1.54	0.16	~ 5	8.08	3.41
WASP-96	G8	5540	12.2	1.06	0.48	8.51	1.20	0.34	8 ± 8	9.28	3.43
HD 209458	G0V	6092	7.65	1.13	0.69	8.48	1.38	0.33	3.5 ± 1.4	8.04	3.50
WASP-17	F4	6650	11.6	1.20	0.51	6.74	1.99	0.08	3 ± 2.6	8.02	3.74
WASP-69	K5	4715	12.4	0.83	0.26	7.48	1.06	0.27	$2 \pm \dots$	11.97	3.87
WASP-39	G8	5400	12.11	0.93	0.28	6.86	1.27	0.17	~ 5	11.68	4.06
HAT-P-1	G0V	5980	10.4	1.15	0.53	8.66	1.32	0.29	$3.6 \pm \dots$	10.19	4.47

Note. Spectral type, stellar temperature in Kelvin, V-band apparent magnitude m_v , stellar mass M_* (in solar masses $M_\odot = 1.9884 \times 10^{33}$ g), planet mass M_p (in Jovian masses $M_J = 1.8983 \times 10^{30}$ g), stellar radius R_* (in planetary radii R_p in Jovian radii $R_J = 7.1492 \times 10^8$ cm), planetary density ρ in g cm^{-3} , stellar age t_* (if unknown, set to average value ~ 5 Gyr), semimajor axis a_p (in stellar radii R_*), and observed period τ_p in days. The tidal Q calculations rely only on these known quantities.

The semimajor axis of a stable exomoon orbiting a close-in gas giant exoplanet of eccentricities e_s and e_p is narrowly confined, $a_s \lesssim 0.49a_H$ ($1.0 - 1.0e_p - 0.27e_s$) (Domingos et al. 2006), at roughly half of the Hill radius, $a_H = a_p \left(\frac{M_p}{3M_*} \right)^{1/3}$. These orbital and observational parameters are computed in Table 2 for a sample of 14 gas giants out to $\sim 10 R_*$. For nearly circular orbits, we find that for $a_s \lesssim 2.3 R_p$, the satellite remains stable, where R_p is the exoplanet transit radius. Table 3 gives a_s and a_H , along with several other length scales such as $R_i = R_p + \delta R_i$, the apparent transit radius at line center due to the presence of a species i , absorbing at resonance wavelength λ_i , adding an apparent change in radius δR_i . The observed absorption depth, $\delta_i = \frac{\Delta \mathcal{F}_{\lambda,i}}{\mathcal{F}_{\lambda,i}}$, reveals the equivalent width, $W_{\lambda,i} = \delta_i \Delta \lambda_i$, where $\Delta \mathcal{F}_{\lambda,i}$ is the fractional change in the stellar flux at line center, and $\Delta \lambda_i$ is the bandpass of the spectrograph. In Section 4.3 we will describe how this information can yield the approximate column density of the absorbing species. As the geometry of the absorbing gas is unknown, spherical symmetry is often assumed while the exoplanet transits a star of radius R_* , so that the absorption depth can also be indicative of the ratio of the effective areas: the absorbing layer (assumed to be an annulus) to the stellar disk, $\delta_i = \frac{R_i^2 - R_p^2}{R_*^2} \sim \frac{2\pi R_p \delta R_i}{\pi R_*^2}$. The Roche radius further confines the satellite's orbit, $R_{\text{Roche}} = 2.456 \left(\frac{\rho_p}{\rho_s} \right)^{1/3}$ (Chandrasekhar 1969), inside which a possible debris disk from a disintegrated satellite could be present, as discussed later in Section 4.

Our study of a tidally locked exoplanet system with planetary orbital period $\tau_{\text{orb}} = \frac{2\pi}{\omega_{\text{orb}}}$ and $\tau_s = \frac{2\pi}{\omega_s}$ will result in a moon orbiting faster than the planet's rotation $\omega_s > \omega_{\text{orb}}$, opposite to the Jupiter-satellite system. When solving the dispersion relation $\omega_s = k^2 \omega_{\text{orb}}$, Wu (2005a, 2005b), Ogilvie & Lin (2004, 2007), and Ogilvie (2014) found that $\omega_s > \omega_{\text{orb}}$, specifically deriving $\tau_s < \tau_{\text{orb}}/2$ as an orbital stability limit due to the lack of tidal dissipation waves into the gas giant's convective envelope from a satellite. The low tidal dissipation \dot{E}_p results in a much higher tidal Q_p , again contrasting the $\omega_s < \omega_{\text{orb}}$ of the Jupiter system of low tidal Q (Lainey & Tobie 2005).

Cassidy et al. (2009) showed that when Q_p is large enough, orbital decay is slow, and the satellite will not be destroyed by tidal decay. That is, the satellite is stable after a time t if $Q_p > Q_{p,\text{crit}}(\tau_{\text{orb}})$, where the critical tidal Q factor for the gas giant based on their Equation (12) is

$$Q_{p,\text{crit}}(t) = c \frac{m_s}{M_p} \left(\frac{1}{\tau_s} \right)^{13/3} t_{\text{dyn}}^{10/3} t. \quad (1)$$

Here m_s and M_p are the satellite and planet masses with dynamical time $t_{\text{dyn}} = 2\pi \left(\frac{R_p^3}{GM_p} \right)^{1/2}$, and $c = 1.9 \times 10^2$. Using Equation (1), an Io-mass satellite in a stable orbit at $2 R_p$ around HD 189733b gives $\tau_s/\tau_{\text{orb}} = 0.18$ and hence is consistent with the use of $\tau_s/\tau_{\text{orb}} = 0.2$ in Cassidy et al. (2009). Therefore, accounting for eccentricities driven by the parent star using Equation (1), an Io-like satellite orbiting a Jovian-mass exoplanet ($m_s/M_p = 4.7 \times 10^{-5}$) for which $t_{\text{dyn}} = 0.12$ days and $\tau_{\text{orb}} = 5\tau_s$ can be sustained beyond a critical orbital period of the planet $\tau_{\text{crit}} = 150 \times (t/Q_{p,\text{crit}})^{3/13}$ for t Gyr. This results in a regime stable to orbital decay for 0.1 and 10 Gyr, as generalized by the solid and dashed lines indicated in Figure 1.

Using the large equilibrium tide value, $Q_{p,\text{crit}} = 10^{12}$ (Goldreich & Nicholson 1977), $\tau_{\text{crit},10 \text{ Gyr}} \gtrsim 0.43$ days, or $\tau_{\text{crit},0.1 \text{ Gyr}} \gtrsim 0.2$ days, much closer-in than our sample of hot Jupiters, as indicated by the shaded regions in Figure 1. All of the observed Na I (red circles) and K I (purple stars) exoplanets reside in a region where an Io-mass exomoon can be dynamically stable throughout the lifetime of the stellar system unless $Q_{p,\text{crit}}$ exceeds Q_p , as given above. Observing an exomoon orbiting within this region of stability would be suggestive of the magnitude of tidal Q . Our calculations in Figure 1 suggest a more moderate range than the equilibrium tide limit of $\sim 10^{12}$, rather a $Q_{\text{J-exoIo,crit}} \sim 10^6 - 10^{10}$ for a hot Jupiter-exo-Io system. The lower tidal Q may explain the lack of robust Na detections for planets outside the inner, $\tau_p \gtrsim 1$ “stable exo-Ios” regime. Since turbulent viscosity increases with heat flux, and the large radii of many hot Jupiters might indicate larger internal heat flux, a more moderate $Q_{p,\text{crit}}$ could be expected.

Given that a stable exomoon orbits at close proximity (Domingos et al. 2006), survival against the gas drag of an

Table 3
Observed Planetary System Parameters

Planetary System	$W_{\lambda,i}$ (mÅ)	T_{eq} (K)	H (km)	τ_i (minutes)	v_{min} (km s $^{-1}$)	R_i (R_p)	R_{Roche} (R_p)	a_{Hill} (R_p)	a_s (R_p)	τ_s (hr)
^a WASP-52b $^{\odot}$	58	1315.00	669	13.0 (3.5)	7.82	1.07	1.11	2.40	1.17	8.40
^b WASP-76b $^{\odot}$	2.78	2190.00	1156	1.4 (0.4)	228.47	1.15	0.97	2.21	1.08	8.69
^c HD 189733b	6.72	1200.00	194	16.9 (4.5)	11.40	1.14	1.69	4.32	2.11	10.65
^d XO-2 N b	20 (10)	1500.00	332	3.8 (1.02)	6.81	1.02	1.60	4.21	2.07	12.56
^e WASP-49b $^{\odot}$	6.05	1400.00	668	4.0 (1.1)	157.57	1.48	1.19	3.56	1.74	13.35
^f HAT-P-12b $^{\odot}$	(160)	960.00	604	26.0 (7.0)	(2.84)	(1.03)	1.14	3.79	1.86	15.42
^g WASP-6b $^{\odot}$	(110)	1150.00	500	5.0 (1.3)	(18.6)	(1.02)	1.19	3.84	1.77	16.13
^h WASP-31b $^{\odot}$	(10)	1580.00	1128	2.8 (0.7)	(59.4)	(1.44)	0.93	3.23	1.58	16.35
ⁱ WASP-96b $^{\odot}$	110	1285.00	559	5.8 (1.5)	6.12	1.02	1.19	4.29	2.10	16.44
^j HD 209458b $^{\odot}$	1.01	1450.00	580	5.7 (1.5)	13.69	1.05	1.17	3.95	1.93	16.80
^k WASP-17b $^{\odot}$	13	1740.00	1961	3.4 (0.9)	240.90	1.35	0.73	2.70	1.28	17.93
^l WASP-69b $^{\odot}$	8.04	963.00	600	35.9 (9.6)	6.47	1.18	1.10	3.97	1.94	18.57
^m WASP-39b $^{\odot}$	0.93 (430)	1120.00	936	6.7 (1.8)	6.54	1.03	0.94	3.66	1.79	19.47
ⁿ HAT-P-1b $^{\odot}$	28 (34)	1322.00	629	8.7 (2.3)	14.95 (12.2)	1.08 (1.10)	1.12	4.65	2.28	21.46

Notes. Here $W_{\lambda,i} = \delta_i \Delta \lambda$, i , the equivalent width in mÅ, is reported directly from the corresponding Na I (*) and low-resolution K I (*) observations if resolved. If not explicitly stated, it is computed based on the spectral resolution $R = \frac{\Delta \lambda}{\lambda}$ and wavelength of Na D2. The T_{eq} is the radiative equilibrium temperature for a zero-albedo surface in Kelvins. The corresponding scale height $H = \frac{k_B T_{\text{eq}}}{\mu m g}$ is computed for a hydrogen/helium envelope. The τ_i alkaline Na I (and K I) lifetime is limited by photoionization using rates from Huebner & Mukherjee (2015) for G stars: $k_{\text{NaD2,G}} = 5.92 \times 10^{-6} \text{ s}^{-1}$. For the F and K stars in our sample, we use $k_{\text{NaD2,F}} = 1.3 \times 10^{-5} \text{ s}^{-1}$ and $k_{\text{NaD2,K}} = 9.5 \times 10^{-7} \text{ s}^{-1}$, the latter being the value adopted for HD 189733b in Huang et al. (2017). The minimum ionization-limited velocity is given by $v_{\text{min}} \sim R_i / \tau_i$, where $R_i = (\delta_i R_*^2 + R_p^2)^{1/2}$ is constrained by the transit depth at line center assuming a spherically symmetric alkaline i envelope as described in the text. For planets with a relatively low R_i , adequate endogenic explanations exist (e.g., Sing et al. 2016; Nikolov et al. 2018). The Roche limit, $R_{\text{Roche}} = 2.456 R_p \left(\frac{\rho_p}{\rho_s} \right)^{1/3}$, is computed for an Io-like satellite of density $\rho_{\text{Io}} = 3.5 \text{ g cm}^{-3}$. The Hill sphere, $a_{\text{Hill}} = a_p (1 - e_p) \left(\frac{M_p}{3M_*} \right)^{1/3}$, and the minimum satellite semimajor axis a_s (in R_p) are computed following Domingos et al. (2006), yielding the corresponding minimum satellite orbital period τ_s in hours.

^a Chen et al. (2017).

^b Seidel et al. (2019).

^c Huitson et al. (2012); Wyttenbach et al. (2015); Khalafinejad et al. (2017).

^d Sing et al. (2011); Sing et al. (2012).

^e Wyttenbach et al. (2017).

^f Barstow et al. (2017); Alexoudi et al. (2018).

^g Nikolov et al. (2014); Barstow et al. (2017).

^h Sing et al. (2015); Gibson et al. (2019).

ⁱ Nikolov et al. (2018).

^j Charbonneau et al. (2002); Snellen et al. (2008); Langland-Shula et al. (2009); Vidal-Madjar et al. (2011); Sing et al. (2016).

^k Barstow et al. (2017); Khalafinejad et al. (2018).

^l Casasayas-Barris et al. (2017).

^m Fischer et al. (2016); Nikolov et al. (2016).

ⁿ Wilson et al. (2015); Sing et al. (2016).

extended and ionized atmosphere should be considered (see Figure 4). At $\sim 2R_J$, the plasma density is $\lesssim 10^7 \text{ cm}^{-3}$ (Huang et al. 2017), where the relative plasma-satellite velocity is $\sim 10 \text{ km s}^{-1}$. Using an expression for the drag force with a drag coefficient that equals 1 (Passy et al. 2012), the time for orbital decay is of the order of $\tau_{\text{drag}} \sim \frac{L}{T}$. Here T is the gas torque from the ionized escaping atmosphere on a satellite with angular momentum L , giving $\tau_{\text{drag}} \gtrsim 200 \text{ Gyr}$, which is a few orders of magnitude longer than the lifetime of the stellar system. Thus, its contribution to orbital decay is negligible. Moreover, we note that while we focus on Io throughout this work, the expected thermal and plasma-driven mass loss described in Section 4 implies that the radius of an Io could erode to an Enceladus-mass satellite affecting the $Q_{p,\text{crit}}$ needed on the order-of-magnitude level, thereby extending the region of stability to closer-in orbits (Figure 1). Given that all alkaline exoplanets can host an Io-mass satellite, in principle, the absorption could be evidence of tidal activity from a satellite. Markedly, a benchmark case of Na I absorption in transmission spectroscopy has been recently observed in Jupiter’s upper atmosphere, presenting the opportunity to evaluate the

endogenic and/or exogenic origin of Na I. In the following, we therefore consider the sources of Na I required to supply the observed line-of-sight (LOS) column density derived from the Na I flux decrease in transit as a guide.

3. Exogenic Sodium in Jupiter’s Atmosphere

Atomic lines of Na I (and several other species, such as Mg I, Fe I, Ca I, Mn I, Li I, and Cr I) were briefly ($< 1 \text{ hr}$) detected in emission from the plumes associated with the impacts of the largest fragments of comet Shoemaker–Levy 9 (SL9) at Jupiter in 1994 July (see review in Crovisier 1996). Most of these emission lines are also observed in the spectra of sungrazing comets, shedding little doubt that the atoms responsible for these atomic lines were present in the impactor itself. Although masses of deposited elements have been quoted in some papers (e.g., Noll et al. 1995), they are quite uncertain because (i) they assume nonsaturated lines, where optical depth effects are difficult to assess and could lead to underestimating the abundances by several orders of magnitude; and (ii) they were derived upon the assumption that resonant fluorescence is

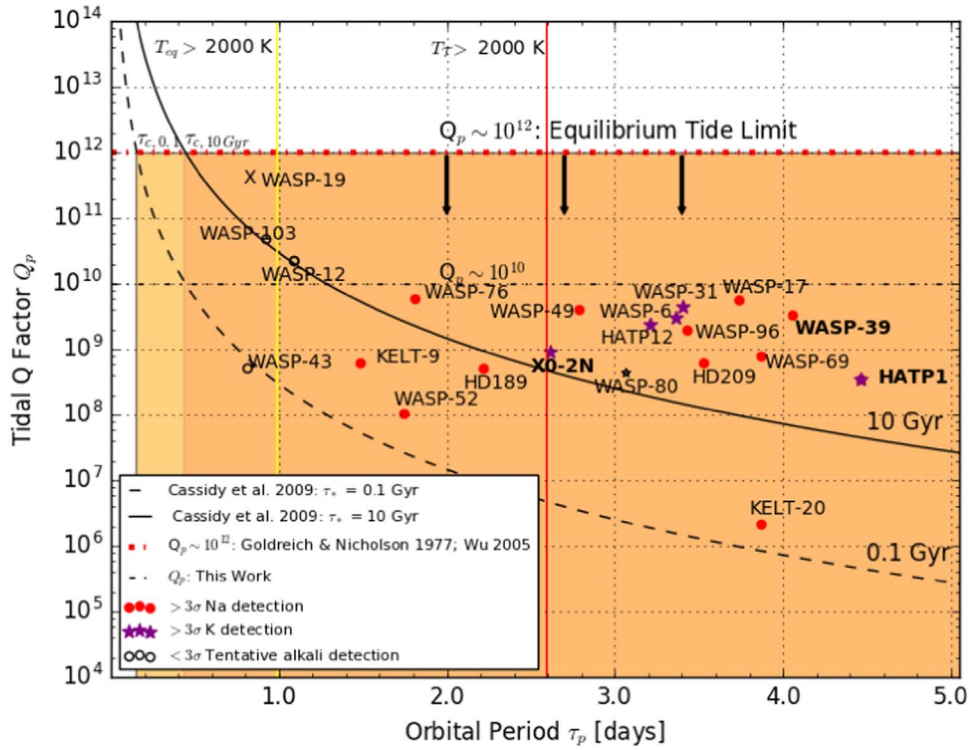


Figure 1. Satellite stability diagram of a close-in gas giant exoplanet system. Shown is the critical tidal Q function $Q_{p,\text{crit}}$ vs. planetary orbital period τ_p for 100 Myr (dashed) and 10 Gyr (solid) gas giant systems. The equilibrium tidal Q_p from Goldreich & Nicholson (1977) and Wu (2005a; horizontal dashed–dotted line), $Q_p \sim 10^{12}$, defines the region of stability, $Q_p > Q_{p,\text{crit}}$, based on the known semimajor axis a_p , stellar age t_* , and an assumed Io-mass satellite. The tidally stable region evolves in time toward larger orbital periods, illustrated from light orange ($\tau_{p,\text{crit}}$ (100 Myr) $\gtrsim 0.2$ day) to dark orange ($\tau_{p,\text{crit}}$ (10 Gyr) $\gtrsim 0.43$ day). The red circles and purple stars show the calculated tidal $Q_{p,\text{crit}}$ for all $>3\sigma$ detections to our knowledge of Na I and K I exoplanetary systems, respectively. The open circles and stars show tentative detections of Na and K, while the large “X” shows that current observations have not detected Na I or K I, yet an atmosphere has been detected. The Na I and K I observations, when examined in conjunction with the tidally stable region, show that all robust detections of Na I and K I exoplanets can host an Io-mass satellite. The current nondetections (i.e., WASP-19b) and the tentative detections at ultrahot Jupiters with high tidal Q s (i.e., WASP-12b, WASP-103b), could suggest a more moderate stability limit, $Q_p \lesssim 10^{11}$, and more conspicuously, also suggest a mass-loss history inside the equilibrium $T_{\text{eq}} \gtrsim 2000$ K and tidal $T_T \gtrsim 2000$ K (Equation (4)) temperature limits computed for a Sun-like star. Within these orbital periods with (red line; $\tau_{p,\text{crit}} \lesssim 2.6$ days) and without (yellow line; $\tau_{p,\text{crit}} \lesssim 1$ day) efficient tidal heating, the extreme mass loss could result in desorbing debris and/or plasma tori. The ultimate survival of exo-Ios is expanded upon in Section 4.

the only excitation mechanism. In reality, other mechanisms, such as thermal excitation by collisions, electronic recombination, and prompt emissions, may also contribute (Crovisier 1996).

Recently, Montañés-Rodríguez et al. (2015; their Figure 4) obtained the first transmission spectrum of Jupiter’s limb by observing an eclipse of Ganymede as it entered Jupiter’s shadow. The observation was carried out with VLT/XSHOOTER at a spectral resolution of $\sim 0.34 \text{ \AA}$. Jupiter’s cold atmosphere at $T \sim 170$ K absorbed $\sim 15\%$ of the planet’s continuum flux at the Na D1 and D2 doublet during transit. This first detection of Na I in Jupiter’s upper atmosphere offers an avenue for endogenic–exogenic comparisons to hot Jupiters. We perform a simple model based on the contribution functions (Figure 3 in Montañés-Rodríguez et al. 2015) at $P_{\text{tot}} = 30$ mbar. For the Na lines, we used spectroscopic parameters kindly provided to us by B. Bézard, including a collisional half-width of $0.270 \text{ cm}^{-1} \text{ atm}^{-1}$ at 300 K. For simplicity, the entire stratosphere above 30 mbar was assumed isothermal at 170 K. Figure 2 shows our modeled spectrum for an LOS Na column density of $7 \times 10^{11} \text{ cm}^{-2}$ fortuitously close to the optically thin column density, $3 \times 10^{11} \text{ cm}^{-2}$, based on the equivalent width $W_{\lambda,i}$ of the spectral line (Equation (14)). Accounting for the Chapman enhancement factor $\sqrt{2\pi \frac{R_j}{H}} \sim 132$, where R_j is Jupiter’s radius and $H \sim 25$ km is the

atmospheric scale height in the region of interest, gives a radial column density of $\sim 5 \times 10^9 \text{ Na cm}^{-2}$ above 30 mbar, i.e., a volume mixing ratio¹⁴ $\text{Na}/\text{H}_2 \sim 10^{-15}$ or $X_{\text{Na}} \sim 10^{-9}$ ppm (demonstrating the extraordinary sensitivity of the lunar eclipse technique by Pallé et al. 2009; Montañés-Rodríguez et al. 2015). We assume below that this mixing ratio holds to deeper levels as a result of vertical mixing.

We note that an Na/H_2 volumetric mixing ratio of 10^{-15} at the 30 mbar level corresponds to a partial pressure of Na of $\sim 3 \times 10^{-17}$ bar. Although the vapor pressure of Na is not well measured at low temperatures, this most likely implies a strong supersaturation of Na. Using the recommended Na vapor pressure expression $P_{\text{sat}}(\text{bar}) = 10^{(5.298 - 5603/T(\text{K}))}$ from the CRC Handbook of Chemistry and Physics (Lide 1994) yields $\sim 2 \times 10^{-28}$ bar at 170 K, implying that the derived partial pressure of $\sim 3 \times 10^{-17}$ bar requires equilibrium at ~ 255 K. Such a temperature is reached in Jupiter’s atmosphere near the 0.25 \mu bar region. If the Na detected by Montañés-Rodríguez et al. (2015) lay in the submicrobar region, the required Na LOS column density would be considerably higher than $7 \times 10^{11} \text{ cm}^{-2}$, because at these lower pressures, pressure

¹⁴ N.B.: Solar abundance $(\text{Na}/\text{H}_2)_{\odot} \sim 10^{-6}$ or $X_{\text{Na},\odot} \sim 1.7$ ppm (Asplund et al. 2009) is assumed in endogenic Na models.

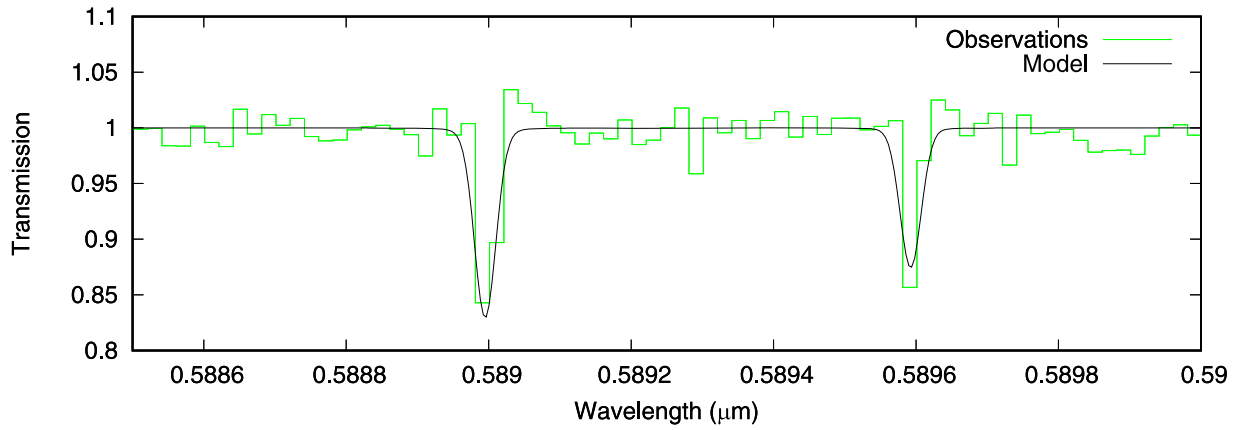


Figure 2. Jupiter’s calculated transmission spectrum in the vicinity of the Na D lines for a tangent level at 30 mbar (black line). The LOS Na column density is $7 \times 10^{11} \text{ cm}^{-2}$, and the spectral resolution is 17,500. The model provides a good match of the observed spectrum (green line) by Montañés-Rodríguez et al. (2015) when Ganymede was in eclipse (their Figure 4).

broadening becomes unimportant, leading to more saturated and narrower lines requiring higher opacities. It is striking, however, that the strongest Na lines observed by Montañés-Rodríguez et al. (2015) occur during the umbra (their Figure 4). This suggests that the bulk of the Na lies in the atmospheric region sampled during the eclipse, i.e., near ~ 30 mbar, and a possibility would be that Na is supersaturated in Jupiter’s stratosphere, perhaps due to inefficient condensation on aerosols.

Gaseous Na observed in Jupiter’s stratosphere is most certainly of external origin, given that any Na-bearing species originating from the interior are expected to condense out in the cold upper troposphere. To assess the external flux required by the observations, we followed the simple approach of Bézard et al. (2002), in which the deposition rate of Na is balanced by its removal from the stratosphere by vertical transport. We used an eddy diffusion coefficient K increasing as $n^{-1/2}$ (where n is the atmospheric number density) above a pressure level $P_0 = 300$ mbar, where K has a minimum value $K_0 = 700 \text{ cm}^2 \text{ s}^{-1}$. Following Bézard et al. (2002; Equation (3)), where the column density of CO above P_0 was derived based on the source flux Φ , we rewrite this expression based on a spherically symmetric mass accretion rate of an exogenic source \dot{M}_{exo} yielding a radial column density

$$N_{\text{exo}} = \frac{\dot{M}_{\text{exo}} H^2}{2\pi R_p^2 m_i K_0}, \quad (2)$$

which corresponds to $\sim 5 \times 10^{10} \text{ Na cm}^{-2}$ above $P_0 = 300$ mbar. Solving for the supply rate, we obtain $\dot{M}_{\text{exo}} \sim 5 \times 10^{-5} \text{ kg s}^{-1}$. This meager mass supply can be understood in terms of the total volatile mass in the envelope. Using the observed column density at 30 mbar, $N_{\text{exo}} \sim 5 \times 10^9 \text{ cm}^{-2}$, we find a total mass of $\approx 1.2 \times 10^5 \text{ kg}$ of Na, integrated over Jupiter. Despite the simplicity of the model, this number is likely accurate to within a factor of a few.

3.1. Exogenic Sources

Possible external sources for the NaI currently observed in Jupiter include (i) the SL9 collision, (ii) past cometary impacts, (iii) micrometeoritic flux, and (iv) NaI escaping from Io’s atmosphere. We demonstrate below that each of these sources is in fact sufficient to account for the above accretion rate \dot{M}_{exo} .

3.1.1. SL9 Impacts

The best-determined amount of materials delivered/produced at Jupiter by the SL9 impacts is for the long-lived species (CO, HCN, CS), as those were both observed just after the impacts (see review Lellouch 1996) and monitored on yearly timescales. The mass of CO produced, in particular, has been estimated to be typically $\sim 5 \times 10^{11} \text{ kg}$ (Lellouch et al. 1997; Moreno et al. 2003), with a probable uncertainty better than a factor of 2. This figure corresponds to $\sim 2.2 \times 10^{11} \text{ kg}$ of atomic O of cometary origin. The Na/O ratio for cosmic abundance can be taken as $\text{Na/O} = 3.6 \times 10^{-3}$ (recommended value from Lodders 2010).¹⁵ Assuming cosmic abundances in SL9 would thus imply a mass of $\sim 8 \times 10^8 \text{ kg}$ of Na deposited by the impacts. Given our estimate of M_{Na} above, it would appear that impacts can easily source the required Na. However, the SL9-delivered material was primarily deposited at the ~ 0.1 mbar level (e.g., Lellouch et al. 1997) and, as of today, it has likely diffused down to pressures of only a few millibars. Thus, a constant Na source today from the SL9 impacts is unlikely, as the Na is observed to be present down to at least 30 mbar.

3.1.2. Older Cometary Impacts

Bézard et al. (2002) showed that CO in Jupiter actually originates from three different components: (i) internal CO, (ii) CO deposited by the SL9 impacts, and (iii) additional stratospheric CO, most likely due to deposition by a suite of “old” cometary impacts with some size distribution for the impactors, which by now has invaded the entire stratosphere. The third component is associated with $\sim 44\text{--}300 \text{ kg s}^{-1}$ of CO. Rescaling the above by the Na/O cosmic ratio suggests that these old impacts would have additionally delivered $\sim 0.13\text{--}0.9 \text{ kg s}^{-1}$ of Na, more than sufficient to explain the equivalent mass of Na observed.

3.1.3. Cosmic Dust

Micrometeoritic flux is also a permanent source of external material, especially oxygen, to the outer planets (see Moses & Poppe 2017 and references therein). These interplanetary dust particles (IDPs) originate from comet activity or disruption,

¹⁵ Lodders indicates $\text{Na/O} = 7.5 \times 10^{-3}$ for chondritic composition and $\text{Na/O} = 3.7 \times 10^{-3}$ in the Sun.

collisions in the asteroid and Kuiper belts, and interstellar dust particles streaming into the solar system. Even though comets are an important source of micrometeorites, an important difference for planetary atmospheres is that micrometeoritic impacts are thought to preserve the H_2O molecules upon entry and ablation, while cometary impacts convert cometary H_2O into atmospheric CO due to shock chemistry. At Jupiter, based on the observed H_2O vertical profile in 1997, which was essentially consistent with expectations from an SL9 source, Lellouch et al. (2002) found that the production of H_2O due to permanent micrometeoritic influx is less than $\sim 1.5 \text{ kg s}^{-1}$, with a best-guess estimated value of $\sim 0.75 \text{ kg s}^{-1}$. This surprisingly low value, compared to expectations from the dynamical dust model of Poppe (2016; who predicted typically 2 orders of magnitude larger fluxes) may suggest that a dominant fraction of the H_2O contained in IDPs is in fact not preserved at micrometeoritic entry. Notwithstanding this poorly understood issue (see also Moses & Poppe 2017), we note that even a scaling of the above H_2O production rate from micrometeorites by the Na/O cosmic abundance yields an Na deposition rate of $\sim 3.7 \times 10^{-3} \text{ kg s}^{-1}$, once again more than sufficient to explain the required Na production rate of $5 \times 10^{-5} \text{ kg s}^{-1}$.

3.1.4. Sodium Accretion from Io

Finally, we calculate the Na I deposition rate on Jupiter from Io, the focus of our work. The accretion rate onto Jupiter, assuming the Na I is escaping isotropically by the physical processes we describe in Section 4 is $\dot{M}_{\text{acc}} \sim \left(\frac{R_j}{a_s}\right)^2 \dot{M}_{\text{Io}}$. For a lower limit to the Na mass-loss rate at Io $\dot{M}_{\text{Io}} \gtrsim 10 \text{ kg s}^{-1}$ and a semimajor axis of $a_s = 5.9 R_j$, the Na accretion rate is 0.1 kg s^{-1} , roughly 2000 times larger than required by the observations. In the anisotropic case, the Na could be collimated into a jet leaving Io at $\sim 3.8 \times 10^{-3} \text{ kg s}^{-1}$ (Schmidt et al. 2015a), which would accrete onto Jupiter at a more moderate rate of $\sim 1.1 \times 10^{-4} \text{ kg s}^{-1}$, yielding the observed mass flux within a factor of 2. We illustrate the physical process of such jets in Figure 3. As discussed below, this source is evidently variable but appears to be quite consistent with the observations. All exogenic sources are capable of supplying considerable amounts of atomic Na I, possibly in excess of the minimum abundance. This may suggest that a dominant fraction of the incoming Na flux is chemically converted to other Na-bearing species, with NaH being a logical candidate.

Besides Na I, recent observations by *Juno* suggest that Io's jets are spraying Jupiter with volatiles based on the detection of sulfur and oxygen ions (S III, O II) in Jupiter's atmosphere at equatorial latitudes (Valek et al. 2018), strongly complementing the exogenic nature of Na we propose. The extreme tidal heating and mass loss at exo-Ios we will now describe may maintain a viable source of Na to a hot Jupiter's upper atmosphere.

4. Exogenic Sodium in Jupiter's Exosphere: Satellite Atmospheric Escape

Io's geologic activity, which results in the ejection of NaCl and KCl into Io's atmosphere, is driven by tidally heated volcanism, whereas the observed and widely distributed Na I and KI are primarily produced by the interaction of the volatiles with the plasma flow in Jupiter's $\sim 4.17 \text{ G}$ magnetic field. The net plasma flow, which governs the momentum and

eventual knockoff of volatiles from the moon, as we will describe, is set by the velocity difference between the plasma torus and the outgassing moon. This feedback process has produced a number of observed alkaline features driven by several molecular physics processes (e.g., Wilson et al. 2002). Although this has resulted in an extensive literature, our focus is on determining the ability of a close-in exoplanetary system to invigorate a volcanic moon and drive a range of possible alkaline source rates to the system by scaling to our robust understanding of the Jupiter–Io system. The resulting column densities can then be directly compared to the observed equivalent widths of alkalis at exoplanets, $W_{\lambda,i}$ (Table 3). We describe the mass loss of Na I and K I at an exo-Io, generalized for a close-in rocky body subject to tidal heating and irradiation. As potassium's signature as a volcanic alkali is similar at Io (Thomas 1996), we focus the following in terms of the robust spectral observations of sodium for simplicity.

4.1. Tidally Driven Volcanism at an Exo-Io

Tidal heating of Io has been shown to be responsible for its widespread volcanism. The tidal heating rate of Jupiter's tidally locked moon, $\dot{E}_s \propto \frac{e^2}{Q_s}$, driven by forced eccentricities, e , locked by Europa and Ganymede's Laplace resonance with Io, is the dominant interior heating source. Similarly, the tidal heating of an exomoon will likely dominate the interior energy budget due to the additional stellar tide. Consequently, the tidal heating rate is orders of magnitude higher than at Io, which for an exo-Io of similar rheological properties ($Q_s \sim 100$, $R_s = R_{\text{Io}}$, $\rho_s = \rho_{\text{Io}}$) can be written as (Cassidy et al. 2009; Equations (19) and (20))

$$\dot{E}_s = \frac{v}{Q_s} \frac{\rho_s^2 R_s^7}{\tau_p^4 \tau_s}, \quad (3)$$

where $v = 3 \times 10^{-7} \text{ cm}^3 \text{ erg}^{-1}$, and $\tau_s = \tau_p/5$ based on the tidal stability criterion discussed in Section 2. For utility, we describe the exo-Io's tidal efficiency as $\eta_T = \frac{\dot{E}_s}{\dot{E}_{\text{Io}}}$, which can readily be computed for any three-body system as tabulated in Table 4. The enhanced tidal heating described in Equation (3) will also contribute to the surface temperature $T_0 = T_{\text{eq}} + \Delta T_0$, which is very roughly approximated as

$$\Delta T_0 = \left(\frac{\dot{E}_s}{4\pi R_s^2 \sigma_{\text{sb}}} \right)^{1/4}, \quad (4)$$

where σ_{sb} is the Stefan–Boltzmann constant and T_{eq} . At Io, the total neutral volcanic content (SO_2 , SO, NaCl, KCl, Cl, and dissociation products) ejected to space (Section 4.2.1) by the incident plasma is estimated to be, on average, $\sim 1000 \text{ kg s}^{-1}$ (e.g., Thomas et al. 2004), varying within an order of magnitude over decades of observations (Burger et al. 2001; Wilson et al. 2002; Thomas et al. 2004). While the source of the dominant gas SO_2 is ultimately tidally driven volcanism, the near-surface atmosphere is mostly dominated by the sublimation of SO_2 frost (Tsang et al. 2016). By observing the atmospheric evolution of the SO_2 column density with heliocentric distance, Tsang et al. (2013) estimated the direct volcanic component to be $N_{\text{volc}} \sim 6.5 \times 10^{16} \text{ cm}^{-2}$, typically $\sim \frac{1}{3}$ of the total observed SO_2 column density. Ingersoll (1989) demonstrated the relative contributions due to both sublimation

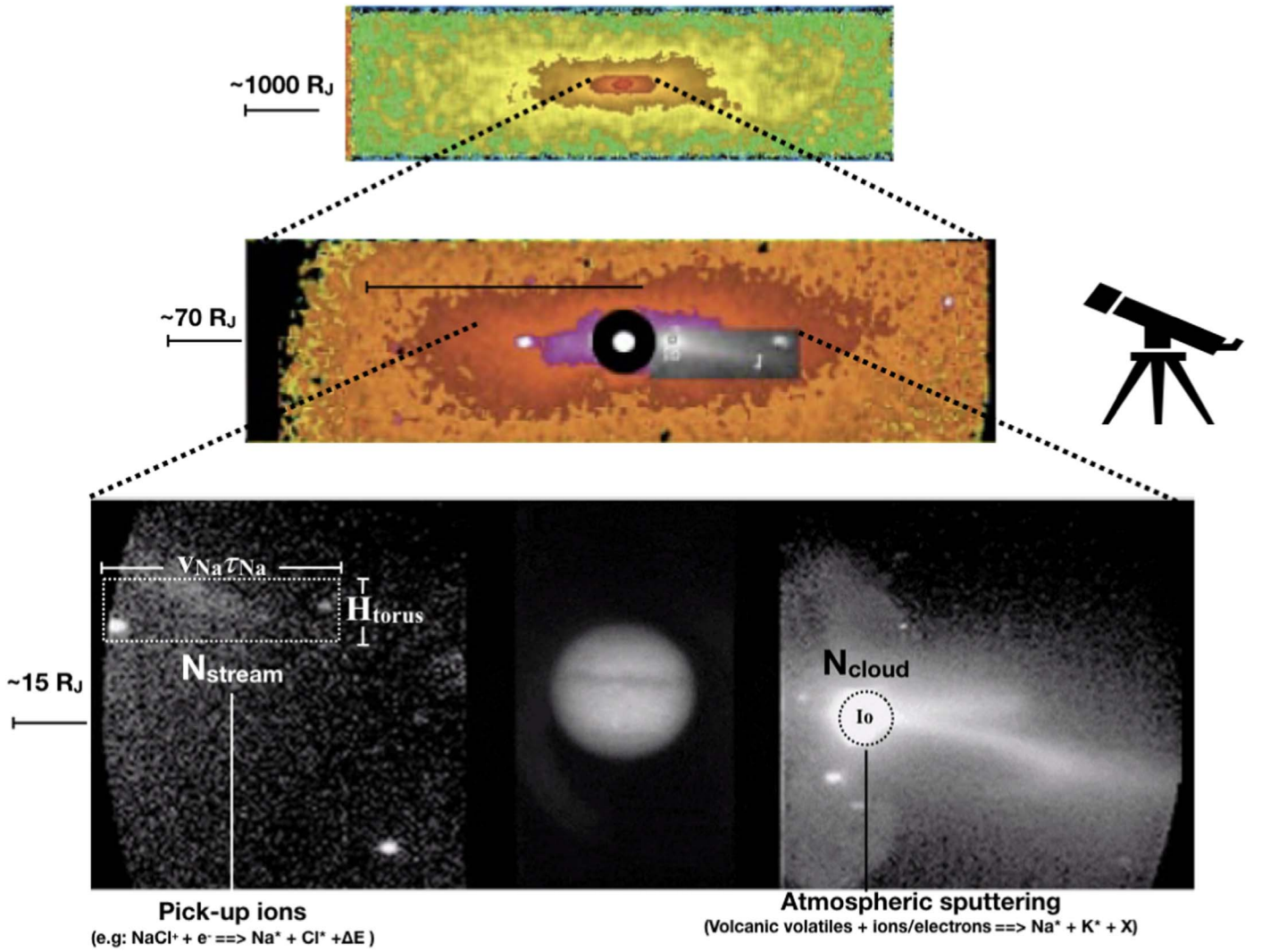


Figure 3. The 2D “face-on” architecture of a sodium exosphere imaged at the Jupiter system. The rectangular Na I exosphere beyond Io at 15, 70, and 1000 R_J is adopted from a 1995 emission observation (Figure 8 of Wilson et al. 2002). In the image sequence at Io’s orbit observed by Schneider et al. (1991), fast Na streams $< 100 \text{ km s}^{-1}$ are seen to emit from the plasma torus. We identify the two principal Na I features at Io’s orbit capable of contributing to a close-in gas giant exosphere: a local cloud and a plasma-driven stream independent of Io’s location. The N_{cloud} at Io (black circle) is driven by atmospheric sputtering at $\sim 10 \text{ km s}^{-1}$, where the radial profile corresponds to Burger et al. (2001; similar to Equation (16)). The N_{stream} on the other side of Jupiter can be derived based on a cross-sectional stream (white rectangle) extended to a length scale $\sim v\tau_{\text{Na}}$, with a height equivalent to that of the ion torus $\sim a_s \frac{v}{v_{\text{orb}}}$ (Johnson & Huggins 2006) driving the stream. An additional “jet” feature is seen near the cloud due to pickup ion neutralization (Wilson et al. 2002; Schmidt et al. 2015a). As described in the text, if the entirety of the Jupiter system were to transit the Sun, the total LOS column density would be $\sim 2.5 \times 10^{10} \text{ Na cm}^{-2}$, easily discernible by current ground-based transmission spectroscopy. An animation of the bottom panel is available. The video shows the neutral sodium evolution in the upper panel and singly ionized sulfur emission in the lower panel demonstrating the gyration of the Io-plasma torus with Jupiter’s magnetosphere. The video duration is 5 s, corresponding to a 10 hr narrowband image sequence observed over a single night by Schneider & Trauger (1995). More information can be found on Apurva Oza’s website under “exo-Io.”

(An animation of this figure is available.)

and volcanic sources in maintaining Io’s atmosphere and established a relationship relating the volcanic source rate to the volcanically supplied atmospheric pressure:

$$P_{\text{volc}} = \frac{v}{\sqrt{32\pi\alpha R_{\text{Io}}^2}} \dot{M}_{0,\text{volc:Io}}. \quad (5)$$

This expression also gives the volcanic column density $N_{\text{volc}} = \frac{P_{\text{volc}}}{m_i g}$, where g is the acceleration due to gravity. Adopting an observed atmospheric temperature of $T_{\text{atm}} = 170 \text{ K}$ by Lellouch et al. (2015) corresponding to an atmospheric scale height of $H = 12 \text{ km}$, a thermal velocity $v = \sqrt{gH}$ equal to 150 m s^{-1} , and a sticking coefficient

$\alpha = 0.5$ for the SO_2 mass of 64 amu yields a volcanic source rate of $\dot{M}_{0,\text{volc:Io}} \sim 6.9 \times 10^6 \text{ kg s}^{-1}$ of SO_2 integrated over Io’s mass M_{Io} . The average volumetric mixing ratio for NaCl to SO_2 at Io is observed to be $X_{\text{NaCl}} \sim 3 \times 10^{-3}$ (Lellouch et al. 2003). This leads to a source rate of $\dot{M}_{0,\text{volc:Io}} \sim 7.4 \times 10^3 \text{ kg s}^{-1}$ of NaCl, somewhat larger than but reasonably consistent with the direct measurement of the NaCl volcanic source rate of $(0.8\text{--}3.1) \times 10^3 \text{ kg s}^{-1}$ (Lellouch et al. 2003). From these estimates, we will adopt $\sim 3 \times 10^3 \text{ kg s}^{-1}$ of Na I as the volcanic source rate for Io.

This source rate is tidally driven. If this source rate was tidally limited with a heating efficiency of 1 (as described further in Section 4.2.3), the implied heating rate is within a

Table 4
Exoplanetary Sodium and Potassium Parameters

Alkaline System	L_{XUV} (erg s $^{-1}$)	f_{mag}	f_{ram}	β	$\eta_{\mathcal{T}}$	T_0 (K)	H_0 (km)	$\lambda_{0,\text{Na}}$	$\mathcal{R}_{\text{SO}_2}$	R_x (R_{Io})	$a_{\text{Hill},s}$ (R_{Io})
Io	1.4×10^{28}	1.0	1.0	1.0	1.0	110	8.3	83	10^{-13}	1.25	5.8
WASP-52b	3×10^{29}	2×10^4	1.8	27	9.5×10^5	2211	160	4.1	10^{-7}	3.2	1.9
WASP-76b	8×10^{27}	3×10^4	0.5	243	8.1×10^5	3049	220	3.0	10^{-11}	4	2
HD 189733b	10^{28}	5×10^2	1.9	6	2.9×10^5	1866	135	4.9	10^{-5}	2.7	2.2
XO-2 N b	8×10^{27}	6×10^2	1.4	13	1.3×10^6	2042	147	4.4	10^{-6}	2.8	2.3
WASP-49b	8×10^{27}	2×10^3	2.3	38	9.4×10^5	1902	137	4.8	10^{-5}	2.6	2.6
HAT-P-12b	3×10^{28}	10^3	2.2	9	4.6×10^5	1379	100	6.6	1	2.1	2.9
WASP-6b	3×10^{27}	10^3	1.6	17	3.6×10^5	1546	112	5.9	10^{-1}	2.3	2.6
WASP-31b	8×10^{27}	3×10^3	1	82	3.4×10^5	1970	142	4.6	5×10^{-6}	2.6	3.0
WASP-96b	5×10^{27}	5×10^2	1.2	24	3.3×10^5	1672	121	5.4	10^{-3}	2.4	3.2
HD 209458b	10^{28}	10^3	1.1	43	3.0×10^5	1827	132	5.0	5×10^{-5}	2.5	2.9
WASP-17b	10^{28}	10^4	0.9	173	2.1×10^5	2087	151	4.3	5×10^{-7}	2.7	3.1
WASP-69b	4×10^{28}	9×10^2	1.7	9	1.8×10^5	1296	94	7.0	1	2.0	3.2
WASP-39b	8×10^{27}	10^3	1.4	25	1.4×10^5	1433	104	6.3	1	2.1	3.4
HAT-P-1b	10^{28}	8×10^2	0.9	30	8.7×10^4	1600	116	5.7	10^{-1}	2.2	3.2

Note. Listed quantities are computed from known stellar quantities in Table 2. The XUV luminosities L_{XUV} are computed from G and K stars from Lammer et al. (2009). The ratios of magnetic and ram pressures at the alkaline planetary system with Io are described as the parameters $f_{\text{mag}} = \frac{P_{\text{mag},p}}{P_{\text{mag},\text{Io}}}$ and $f_{\text{ram}} = \frac{P_{\text{ram},p}}{P_{\text{ram},\text{Io}}}$, where $P_{\text{mag},\text{Io}} = 1.5 \times 10^{-5}$ dyne cm $^{-2}$ and $P_{\text{ram},\text{Io}} = 2.4 \times 10^{-6}$ dyne cm $^{-2}$. The canonical ratio of radiation pressure acceleration to gravity, β , is estimated using the parameters in Table 2. The satellite β_s is additionally defined in Equation (15). The tidal efficiency $\eta_{\mathcal{T}}$ with respect to Io is the ratio of tidal dissipation rates $\dot{E}_s/\dot{E}_{\text{Io}}$ as in Equation (3). The net surface temperature including tidal heating is T_0 as in Equation (4). The scale height evaluated at T_0 for the volcanic volatile SO_2 is listed as H_0 . The Jeans parameter for Na is λ_0 . The conduction prefactor $\mathcal{R}_{\text{SO}_2}$ describes the suppressed surface Jeans escape of the entire atmosphere as in Equation (12). The exobase radius as defined in Equation (8), R_x , is in units of Io radii: $R_{\text{Io}} = 1822$ km. As described in the text, the exobase for Na is derived using the observed SO_2 density at the surface $n_{0,\text{SO}_2} = 1.8 \times 10^{11}$ cm $^{-3}$ (Lellouch et al. 2015) and mixing ratio $X_{\text{NaCl}} = 0.013$ (Lellouch et al. 2003) based on venting from the surface.

factor of ~ 5 of Io's theoretically derived $\dot{E} = 1.6 \times 10^{19}$ (Peale et al. 1979), validating the ability of $\eta_{\mathcal{T}}$ to probe a supply rate efficiency.

4.2. Exo-Io Mass-loss Processes: Exogenic Sodium and Potassium Sources in an Exoplanet Magnetosphere

Moons are well known to be significant plasma sources in gas giant magnetospheres (Johnson et al. 2006a, 2006b). At Io, the ejected species are eventually ionized by the plasma and radiation environment, forming a toroidal plasma corotating with the Jovian magnetic field that has been remarkably imaged in a sequence of S II and O II spectra gyrating with Jupiter's B field (see Figure 1 Schneider et al. 1991) and its corresponding Na features, which we identify in the context of an exo-Io transit in Figure 3. The plasma interaction with Io's upper atmosphere produces a number of distinguishable Na features produced by a multitude of physical processes, including ion-neutral momentum transfer, charge exchange, and dissociative recombination of NaCl^+ , as analyzed and simulated by Wilson et al. (2002). In Figure 3, we identify three principal Na features in Jupiter's exosphere, all ultimately Iogenic:¹⁶ cloud, stream, and nebula. At an exoplanet, these features are averaged over the planet's transit duration and are spatially unresolved. Therefore, an estimate of the LOS column density independent of the spatial distribution is needed during an exoplanet transit. The average LOS column density $\langle N \rangle$ is simply the total number of atoms \mathcal{N} in the system, which is obtained by integrating the LOS column over the surface area of the star:

$$\langle N \rangle = \frac{\mathcal{N}}{\pi R_*^2}. \quad (6)$$

As a thought experiment, the average Na I column density an external observer would notice if Jupiter's exosphere ($\sim 1000 R_J$)

were transiting the Sun is $\sim 2.5 \times 10^{10}$ Na cm $^{-2}$. This quantity, using the inset image from Figure 3, is within a factor of 3 of Jupiter's atmospheric sodium (Section 3).

At a close-in exoplanet system, the total quantity of Na atoms can be estimated based on a model of tidally driven mass loss and ionization, as we will describe in Section 4.3. Due to ionization and tidal heating, the close stellar proximity will simultaneously compactify the overall Na exosphere by $\propto \frac{1}{a_p^2}$ and magnify the overall Na source rate by $\propto a_p^{15/2}$. Furthermore, as we will describe, the minimum observed quantity of Na atoms can also be estimated if the equivalent width of the spectral line is resolved in high-resolution transmission spectroscopy.

Due to the tilt of the magnetic equator to Io's orbit and the variation in the sourcing, these features are also variable. Only recently has a magnetic field been observed around substellar bodies: L and T dwarfs (Kao et al. 2018). While an exoplanetary magnetic field is expected, it is still unconstrained (Grießmeier et al. 2007; Christensen et al. 2009; Kislyakova et al. 2014; Matsakos et al. 2015; Rogers 2017). The activity from the type of satellite we describe here could be used to indicate the presence of such a field. It is clear that a description of the magnetospheric environment is needed before assessing the nature of the Na I and K I absorption features seen at hot Jupiters. Due to the shorter photoionization lifetime of the alkalis at a close-in exoplanet (τ_i ; Table 3 scaled to Huebner & Mukherjee 2015), the Na I features seen at an exo-Io would be far smaller than the imaged Jovian system (Figure 3). For example, assuming a spherically symmetric endogenic Na I cloud of apparent radius $R_{\text{Na}} \sim 1.14 R_p$ (see Table 3) about the exoplanet HD 189733b corresponds to an absorbing layer of area $\sim 6 \times 10^{19}$ cm 2 compared to Jupiter's magnanimous Na I cloud $\sim 10^{24}$ cm 2 evaluated at radius $70 R_J$. If Jupiter were close-in, the photoionization time would significantly reduce this area to $\pi R_c^2 \sim \pi (v_i \tau_i)^2 \sim 3 \times 10^{18}$ cm 2 when considering

¹⁶ Sourced by Io.

an NaI cloud outgassed at $v_i \sim 10 \text{ km s}^{-1}$ due to an exo-Io (Johnson & Huggins 2006). In the following, guided by molecular kinetic simulations and Io observations described above, we estimate an exo-Io's NaI escape rate based on its volcanic gas source rate. This will provide rough lower limits on possible alkaline column densities based on our knowledge of tidal heating and thermal desorption from a close-in rocky body.

We will rely on molecular kinetic simulations and Io's observations described above to estimate an exo-Io's NaI escape rate based on its volcanic gas source rate to provide rough lower limits on possible alkaline column densities based on our knowledge of tidal and thermal heating, relevant for a close-in rocky body. In all scenarios, we self-consistently include the expected tidal heating based on the above discussion. We focus on three principal drivers of atmospheric escape described in Johnson et al. (2015) and Johnson (2004).

4.2.1. \dot{M}_p Plasma-driven Escape: Atmospheric Sputtering of an Exo-Io

Io's volcanic mass loss is due to momentum exchange with the incident plasma and is often referred to as atmospheric sputtering (Haff et al. 1981). Here sputtering is used as a proxy to account for net loss due to the ambient plasma and its accompanying fields. Scaling to the plasma pressure at Io, $P_{\text{Io}} \sim 1.8 \times 10^{-5} \text{ dyne cm}^{-2}$ (Johnson 1990), one can derive the tidally driven atmospheric sputtering of atomic NaI at an exomoon building on Johnson (2004) as

$$\dot{M}_p \sim x_i \frac{P_s}{P_{\text{Io}}} \frac{U(R_x)_{\text{Io}}}{U(R_x)_s} \frac{R_{x,s}^2}{R_{x,\text{Io}}^2} \dot{M}_{\text{Io}}, \quad (7)$$

which is scaled to Io's measured mass-loss rate, $\dot{M}_{\text{Io}} \sim 1000 \text{ kg s}^{-1}$. This is generalized for a volatile species i , where x_i is the mass fraction. For atomic sodium, the mass fraction is set to 0.1 in the exobase region using the 1995 Na I emission (Figure 3) based on the total SO_2 mass. P_s is the plasma pressure at the extrasolar satellite, and $U(R_x)$ is the satellite's gravitational binding energy at its exobase of radius, $R_{x,s}$. A lower bound to the exobase for an exponential atmosphere with a scale height H_0 determined by the surface temperature and a surface density, n_0 , that is enhanced by the extreme tidal heating is

$$R_{x,s} \sim R_s + H_0 \ln(n_0 H_0 \sigma_i). \quad (8)$$

Here R_s is the satellite radius, H_0 is the volcanic (SO_2) scale height at the tidally heated surface temperature T_0 , and σ_i is the collisional cross section¹⁷ between the escaping alkaline species and ambient atmosphere. Table 4 tabulates the lower and upper bounds to the exobase for an exponential atmosphere.

Since the loss due to ionization occurs in the exobase region, in Equation (8), we use, for simplicity, $n_0 \sim \frac{\tau_{\text{Na,exo-Io}}}{\tau_{\text{Na,Io}}} x_{\text{Na}} \eta_T n_{0,\text{SO}_2}$, where $\frac{\tau_{\text{Na,exo-Io}}}{\tau_{\text{Na,Io}}}$ accounts for rapid ionization at an exo-Io based on Io's Na lifetime of $\tau_{\text{Na,Io}} \sim 4 \text{ hr}$, and η_T is a factor accounting for the enhanced tidal heating (Equation (3)). This heating would enhance the surface column density at Io, which we approximate here as the product of the surface number density $n_{0,\text{SO}_2} = 1.8 \times 10^{11} \text{ SO}_2 \text{ cm}^{-3}$ and the scale height (Lellouch et al. 2015).

We use a near-surface mixing ratio of $X_{\text{Na}} = 0.013$ from the direct detection of NaCl accounting for venting (Lellouch et al. 2003).

Io's exobase is $\sim 465 \text{ km}$ or $\approx 1.25 R_{\text{Io}}$ (Wong & Johnson 1996a, 1996b; McDoniel et al. 2017), whereas the observed NaI profile is far more extended and not exponential (see Section 5.2.3) and Burger et al. 2001). Such an atmospheric tail is not unlike that for a comet or disintegrating rocky body, as we describe in Section 4.2.3. However, the exobase altitude is limited by its Hill sphere so that $R_{x,s} \sim a_{\text{Hill},s}$ in which case the satellite atmosphere experiences Roche lobe overflow. The satellite Hill radius $a_{\text{Hill},s} \sim a_s \left(\frac{M_{\text{Io}}}{3M_p} \right)^{1/3}$ is tabulated in Table 4, where the exo-Io is assumed to be in a circular orbit of semimajor axis a_s (see Table 2).

The plasma pressure at the exobase can be roughly written as $P_p = P_{\text{mag}} + P_{\text{thermal}} + P_{\text{ram}}$, where the magnetic and ram pressures dominate at Io. Therefore, a lower bound at an exo-Io is obtained using $P_s \sim P_{\text{mag}} + P_{\text{ram}} \sim \frac{B_r^2}{2\mu_0} + n_i m_i (u_i)^2$, where B_r is the planetary magnetic field strength at the orbit of the satellite; μ_0 is the permeability of the vacuum; and n_i , m_i , and u_i are the ion number density, average mass, and ion flow speed, respectively. At an exo-Io, the pressure could be larger based on the unknown magnetic field strength of the gas giant. As a lower limit, we assume an unmagnetized gas giant where, in Table 4, we calculate the ram pressure at each exoplanet based on Parker's solar wind model (Parker 1964), scaling to the ion density at 1 au. We find that in the unlikely absence of a magnetic field on the gas giant, a satellite would experience a stellar wind ram pressure comparable to the ram pressure at Io's exobase, as indicated by the parameter f_{ram} (Table 4). As an upper limit, we assume a Jovian-like B field leading to a large magnetic pressure, as is the case at Io. At an exo-Io $\sim 2 R_p$ away, the magnetic pressure is ~ 700 that at Io, as indicated by the parameter f_{mag} (Table 4). We find that plasma-driven loss dominates at most alkaline systems, with the exception of five systems, WASP-52b, WASP-76b, and HD 189733 b (energy-limited escape), as well as WASP-69b and HAT-P-12b (thermal evaporation), driven by the mechanisms we shall now describe.

4.2.2. \dot{M}_U : Energy-limited Escape from an Exo-Io

We evaluate the simple energy-limited escape (Watson et al. 1981) regime shown to dominate the close-in exoplanet atmospheric escape in the *Kepler* data (Jin et al. 2014; Fulton & Petigura 2018). Due to the extreme irradiation at a close-in gas giant, the incoming UV and X-ray (XUV) radiation will heat the upper atmosphere of the outgassing exo-Io. The heating will expand the gas and result in hydrodynamic escape, which is typically approximated as

$$\dot{M}_U \sim m_i x_i \frac{Q}{U_s(R_a)}, \quad (9)$$

where $Q = \eta_{\text{XUV}} 4\pi R_a^2 F_{\text{XUV}}$ is the heating rate due to the incident XUV flux F_{XUV} , R_a is the radius at which the bulk of XUV radiation is absorbed, m_i is the volatile mass, x_i is the mass fraction, and U_s is the binding energy as described in Johnson et al. (2015) for small bodies. Absorption in the upper atmosphere should be efficient due to the presence of volcanic molecules. In Jin & Mordasini (2018), a heating efficiency of 0.1 is used for H/He atmospheres, and for Io's volcanically generated atmosphere, Lellouch et al. (1992) used a heating

¹⁷ For the dominant volcanic species, we use $\sigma_{\text{SO}_2} = 1.62 \times 10^{-14} \text{ cm}^2$.

efficiency of 0.35. To account for both the expansion of the atmosphere and the heating efficiency, for simplicity, we use $R_a \sim R_s$ and $\eta_{\text{XUV}} = 0.1\text{--}0.4$ (see Murray-Clay et al. 2009). We caution that the escape flux may be further reduced due to transonic escape, which occurs when $Q > Q_c$ (see Equation (10) and Figure 2 of Johnson et al. 2013). If Q is too large, the escape is limited by the surface source rate, which we describe below.

4.2.3. \dot{M}_S Source-limited Escape: Thermal Evaporation of an Exo-Io

Due to the extreme tidal heating and irradiation, thermal escape at an exo-Io may also contribute to the total NaI and KI mass loss. Based on the surface T_0 , we compute two possible surface source rates as at Io: $\dot{M}_{0,\text{evap}}$ and $\dot{M}_{0,\text{volc}}$. Improving upon previous calculations (Equation (36) of Cassidy et al. 2009, derived from Fegley & Cameron 1987), we use the experimentally derived values of van Lieshout et al. (2014), based on the Arrhenius-type vapor pressure relation $P_{\text{vap}} = \exp(-A/T_0 + B)$ (Equation (13) of van Lieshout et al. 2014), where we use the average of two rocky mineral end members, enstatite MgSiO_3 : $A = 68,908 \pm 8773$ K; $B = 38.1 \pm 5.0$ and fayalite Fe_2SiO_4 : $A = 60,377 \pm 1082$; $B = 37.7 \pm 0.7$. The source rate due to thermal evaporation can be written as

$$\dot{M}_{0,\text{evap}} = x_i 4\pi R_s^2 P_{\text{vap}}(T_0) \left(\frac{m_i}{2\pi k_b T_0} \right)^{1/2}, \quad (10)$$

where m_i is the mass of the volatile atom or molecule in question and x_i is the mass fraction. We use a lower limit to the chondritic composition of Io constrained by Fegley & Zolotov (2000) to be $x_{\text{Na}} = 0.05$. Based on the variety of Na/K ratios in Table 1, it is conceivable that x_{Na} will vary over time, and further geophysical modeling assessing interior-atmosphere coupling is needed (e.g., Noack et al. 2017; Bower et al. 2019).

The tidally limited volcanic source rate for an exo-Io can be roughly estimated as $\sim \eta m_i \frac{\dot{E}_t}{U_i}$ based on Equation (3) with an efficiency η . In Section 4.1, based on direct observations of the volcanic species NaCl and SO_2 , we validated the tidally driven NaI supply at Io. Directly scaling to this supply, albeit variable, we can write the tidally driven volcanic source rate at an exo-Io as

$$\dot{M}_{0,\text{volc:Exo-Io}} \sim \eta_T \dot{M}_{0,\text{volc:Io}}. \quad (11)$$

The total source rate, like at Io, is evaporative and volcanic: $\dot{M}_0 \sim \dot{M}_{0,\text{evap}} + \dot{M}_{0,\text{volc}}$. Therefore, the source-limited escape rate due to surface heating for a given species of surface Jeans parameter $\lambda_0 = \frac{Gm_i m_i}{R_s k_b T_0}$ can be written as

$$\dot{M}_S = \mathcal{R} \dot{M}_0 (1 + \lambda_0) \exp(-\lambda_0), \quad (12)$$

where \mathcal{R} depends on n_0 , the surface density of the species following Equation 2(A) in Johnson et al. (2015),¹⁸ where σ_i is the collisional cross section of the escaping species in question, typically $\sim 10^{-15} \text{ cm}^2$ for N_2 in the molecular kinetic simulations from Volkov & Johnson (2013) to which the parameter is fit. This estimate is, in principle, more accurate than the standard Jeans escape used in the literature, as it includes the suppressed escape due to Fourier conduction, as demonstrated in recent molecular kinetic simulations of volatile escape at

small bodies (Volkov et al. 2011; Volkov & Johnson 2013; Johnson et al. 2015). In Table 5, we consider the evaporation timescale of the entirety of an exo-Io (composed of $\text{MgSiO}_3\text{--Fe}_2\text{SiO}_4$) by focusing only on the total source-limited escape described above as a first approximation.

Finally, we estimate $t_{\text{evap}} \sim \frac{\dot{M}_{\text{Io}}}{\dot{M}_{S,\text{tot}}}$, the critical timescale to evaporate the entirety of the exo-Io. As a rough bound to the silicate component of the exo-Io, we assume the total loss eroding the surface is $\dot{M}_{S,\text{tot}} \sim \dot{M}_S$, where $x_i = 1.0$. As the evaporation timescale describes the entirety of the exo-Io describing the silicate evaporation of MgSiO_3 and Fe_2SiO_4 , we consider only source-limited escape (Equation (12), improved from Jeans escape). We find that for several candidate systems, less than 1% of an exo-Io would have evaporated throughout the stellar lifetime (t_* ; Table 2), which we have shown in bold based on our range of mass-loss rates. We flag potentially disintegrated exo-Io systems from our mass-loss model as \odot and the $T_0 \gtrsim 2000$ K catastrophic disintegration from Perez-Becker & Chiang (2013) as \bigcirc . The large uncertainties in stellar age permit the possibility that several of these flagged systems still have an Io-mass satellite today. While we have modeled the principal mass-loss processes, these estimates should only be used as a guide, as more detailed modeling is needed to assess the fate of these systems. That is, we have assumed that the rheological properties of the moons are similar to Io's, yielding the tidally heated surface temperatures (Table 4; T_0) dominating the putative satellite destruction. Figure 1 additionally marks the critical destruction limit for Sun-like systems using Equation (4) at $T_0 = T_{\text{eq}} + \Delta T_0$ (yellow) and $T_0 = T_{\text{eq}}$ (red).

Satellite destruction implies a large source of circumplanetary material, possibly in the form of a planetary ring (e.g., Burns et al. 1999) or gas torus (Johnson & Huggins 2006) capable of generating alkaline signatures due to the extreme photodesorption. Saturn's stable toroidal atmosphere of O_2 is supplied purely by the photodesorption and sputtering of ice grains in its planetary ring (Johnson et al. 2006a). A lower limit to desorption from such debris is provided in Table 5 as $\langle \dot{M}_0 \rangle_d$, which also serves as a lower limit for a desorbing Trojan source with negligible tidal heating. Dust signatures from a catastrophically disintegrating body appear to be rare, as is the case for the planetary systems at the anomalous stars KIC 12557548, KIC 8462852, RZ Piscium, and WD 1145+017 (Rappaport et al. 2012; Vanderburg et al. 2015; Boyajian et al. 2016; Punzi et al. 2018). Nonetheless, the fact that all strongly outgassing alkaline systems have sub-Saturnian densities (Table 3; \odot) may suggest a close-in torus of exogenic material (Zuluaga et al. 2015).

As a final step, we take the net mass-loss rates $\dot{M}_{\text{Exo-Io}}$, translate them to the NaI supply rates for the exoplanetary system, and compute the LOS column densities averaged over the entire stellar disk (Equation (6)) shown in Table 5:

$$\langle N \rangle_{\text{Exo-Io}} = \frac{\langle \dot{M}_{\text{Exo-Io}} \rangle_{\tau_i}}{\pi R_*^2 m_i}. \quad (13)$$

Here $\dot{M}_{\text{Exo-Io}}$ is the dominant mass-loss rate based on the three mechanisms we compute: source-limited \dot{M}_p (Equation (7)), energy-limited \dot{M}_p (Equation (7)), and plasma-limited \dot{M}_p (Equation (7)) in Table 5. Therefore, the total number of absorbers \mathcal{N} along an LOS is limited by the alkaline lifetime so that $\mathcal{N} \sim \frac{\dot{M}_{\text{Exo-Io}}}{m_i} \tau_i$, where τ_i is assumed to be limited by ionization.

¹⁸ $\mathcal{R} = ((n_0 \sigma R_s)^{-0.09} + (0.014 n_0 \sigma R_s \lambda_0^{2.55} \exp(-\lambda_0)))^{-1}$.

Table 5
Candidate Exo-Io Sodium and Potassium Mass-loss Calculations

Exo-Io	$\langle \dot{M}_0 \rangle_{\text{evap}}$	$\langle \dot{M}_0 \rangle_{\text{volc}}$	$\langle \dot{M}_0 \rangle_d$	$\langle \dot{M}_S \rangle$	$\langle \dot{M}_U \rangle$	$\langle \dot{M}_P \rangle$	$^* \langle N \rangle_{\text{K,Exo-Io}}$	$^* \langle N \rangle_{\text{Na,Exo-Io}}$	$\langle N \rangle_{\text{Obs}}$	$\langle t \rangle_{\text{evap}}$	$\langle f_{\text{loss}} \rangle$
	(kg s ⁻¹)	(kg s ⁻¹)	(kg s ⁻¹)	(kg s ⁻¹)	(kg s ⁻¹)	(kg s ⁻¹)	(K cm ⁻²)	(Na cm ⁻²)	(Na cm ⁻²)	(Gyr)	$\frac{t_*}{t_{\text{evap}}}$
○ WASP-52b I	10 ^{12.1±0.8}	10 ^{9.4±1}	10 ^{3.6±1.4}	10 ^{2.6±1}	<i>10^{6.8±2}</i>	10 ^{4.7±1.9}	10 ^{11.2±1}	10 ^{13±1}	10 ^{11.5±0.05}	360 ± 60	1.1e-3 ± 8e-4
○ WASP-76 b I	10 ^{15.5±0.5}	10 ^{9.3±1}	10 ^{12±0.8}	10 ^{2.9±1}	<i>10^{5.1±2.6}</i>	10 ^{4.7±2.2}	10 ^{7.8±.6}	10 ^{9.6±.6}	10 ^{10.1±0.05}	180 ± 35	2.82e-2 ± ...
HD 189733 b I	10 ^{9.8±1}	10 ^{8.9±1}	10 ^{1.6±1.5}	10 ^{2.8±.3}	<i>10^{5.4±0.2}</i>	10 ^{4±1.2}	10 ^{9.8±.5}	10 ^{11.6±.5}	10 ^{10.4±0.05}	230 ± 110	1.9e-2 ± 1e-2
○ XO-2 N b I	10 ^{11.1±0.9}	10 ^{8.5±1}	10 ^{6.2±1.2}	10 ^{2.5±1}	10 ^{5±0.2}	<i>10^{4±1.3}</i>	10 ^{8.6±.5}	10 ^{10.5±.5}	10 ^{11±0.05}	430. ± 64	1.5e-2 ± 6e-3
WASP-49 b I	10 ^{10.1±1}	10 ^{8.4±1}	10 ^{4.9±1.3}	10 ^{2.5±1}	10 ^{5±0.2}	<i>10^{4.3±1.5}</i>	10 ^{8.6±.4}	10 ^{10.4±.4}	10 ^{10.7±0.05}	400. ± 30	1.3e-2 ± ...5
○ HAT-P-12b I	10 ^{4.6±1.3}	10 ^{8±1}	10 ^{-4.2 ± 1.9}	<i>10^{5.8±.9}</i>	10 ^{5.6±0.2}	10 ^{4.2±1.6}	10 ^{10.6±.7}	10 ^{13.3±.2}	...	0.20 ± 0.18	13 ± 10
○ WASP-6 b I	10 ^{6.7±1.1}	10 ^{8±1}	10 ^{0.6±1.6}	10 ^{4.1±1.1}	10 ^{4.5±0.2}	<i>10^{4.2±1.7}</i>	10 ^{9±.3}	10 ^{11.1±.1}	...	12 ± 10	0.9 ± 0.6
WASP-31 b I	10 ^{10.6±0.9}	10 ^{7.9±1}	10 ^{7.1±1.2}	10 ^{2.5±0.1}	10 ^{4.8±0.2}	<i>10^{4.3±1.9}</i>	10 ^{8.1±.7}	10 ^{9.9±.7}	...	470 ± 70	1.1e-2 ± ...
WASP-96 b I	10 ^{8.1±1.1}	10 ^{7.9±1}	10 ^{3.1±1.4}	10 ^{3.1±.6}	10 ^{4.6±0.2}	<i>10^{4±1.6}</i>	10 ^{8.3±.5}	10 ^{10.3±.5}	< 10 ^{11.7±0.05}	110 ± 84	7.3e-2 ± 7e-2
HD 209458 b I	10 ^{9.5±1.0}	10 ^{7.9±1}	10 ^{3.4±2.4}	10 ^{2.5±0.1}	10 ^{5±0.2}	<i>10^{3.8±2.7}</i>	10 ^{8.6±.1}	10 ^{10.4±.1}	10 ^{9.7±0.05}	410 ± 56	8.5e-3 ± 3e-3
○ WASP-17 b I	10 ^{11.4±0.9}	10 ^{7.7±1}	10 ^{8.7±1.1}	10 ^{2.5±1}	10 ^{5±0.2}	<i>10^{4.6±2.2}</i>	10 ^{8.3±.8}	10 ^{10.1±.8}	10 ^{10.8±0.05}	422. ± 80	7.1e-3 ± 6e-3
○ WASP-69 b I	10 ^{3.3±1.4}	10 ^{7.6±1}	10 ^{-4.1 ± 1.9}	<i>10^{5.9±.3}</i>	10 ^{5.6±0.2}	10 ^{4±1.7}	10 ^{10.3±.1}	10 ^{13±.1}	10 ^{10.7±0.05}	0.18 ± 0.08	11 ± ...
○ WASP-39 b I	10 ^{5.3±1.3}	10 ^{7.5±1}	10 ^{-0.1 ± 1.7}	10 ^{4.9±1.1}	10 ^{4.8±0.2}	<i>10^{4.2±1.8}</i>	10 ^{9.3±.4}	10 ^{11.7±.2}	10 ^{9.7±0.05}	1.8 ± 1.7	2.8 ± ...
HAT-P-1b I	10 ^{7.3±1.1}	10 ^{7.3±1}	10 ^{3.7±1.4}	10 ^{3.2±.7}	10 ^{4.8±0.2}	<i>10^{4.1±1.6}</i>	10 ^{8.6±.8}	10 ^{10.6±.8}	10 ^{11.2±0.05}	91 ± 74	3.9e-2 ± ...

Note. Order-of-magnitude estimates to assess the plausibility of an exo-Io source at each alkaline exoplanetary system. Here $\langle \dot{M}_0 \rangle_{\text{evap}}$ (Equation (10)) and $\langle \dot{M}_0 \rangle_{\text{volc}}$ (Equation (11)) are the Na I source rates at T_0 (Equation (4)) due to thermal evaporation and volcanism, respectively. For thermal evaporation, we consider a range of mineral vapor pressures bounded by MgSiO₃ and Fe₂SiO₄. For tidally driven volcanism, our results are scaled to Io for a range of tidal efficiencies η_T corresponding to ≈ 2 dex in rheology parameters. Here $\langle \dot{M}_0 \rangle_d$ is a lower bound to thermal evaporation (Equation (12)) evaluated at the equilibrium temperature T_{eq} with a null value of tidal heating $\dot{E}_s = 0$ (Equation (3)). The subsequent mass-loss ranges $\langle \dot{M}_S \rangle$ (Equation (12)), $\langle \dot{M}_U \rangle$ (Equation (9)), and $\langle \dot{M}_P \rangle$ (Equation (7)) are provided for completeness considering three principal mechanisms: surface heating, upper atmospheric heating, and plasma heating, respectively. For $\langle \dot{M}_S \rangle$, the source-limited escape is directly limited by $\langle \dot{M}_0 \rangle$ and strongly dependent on conduction to the surface, as described by \mathcal{R} and provided in Table 4. For $\langle \dot{M}_U \rangle$, the upper atmosphere/energy-limited escape depends on the incident L_{XUV} radiation at the star derived from Lammer et al. as in Jin & Mordasini (2018), where we consider heating efficiencies between 0.1 and 0.4. Due to the extreme irradiation, we note that it is likely that this rate is an upper limit (Johnson et al. 2013). For $\langle \dot{M}_P \rangle$, the plasma-limited escape depends strongly on the exobase radius and the incident plasma pressure P_s , where our lower bound is stellar wind-limited and the upper bound includes the magnetic pressure of the gas giant (see Table 4 and Table 4.1 of Johnson 1990). The maximum mass-loss rates are italicized based on the upper limits. The predicted average exo-Io column density based on the principal mass-loss source for Na I (\bullet) and K I (\star) is provided as $\langle N \rangle_{\text{Exo-Io}}$ (Equation (13)) and directly compared to the derived column from transmission spectroscopy observations $\langle N \rangle_{\text{Obs}}$ (Equation (14)). The range of values from transmission spectroscopy is tightly constrained, as the equilibrium optical depth is fundamentally $\tau \sim 1$, although the equivalent width can indeed vary. Systems where $\langle N \rangle_{\text{Exo-Io}} < \langle N \rangle_{\text{Obs}}$ are flagged as problematic for an exogenic lunar source. The evaporation timescale for the exo-Io t_{evap} is estimated based on our knowledge of the surface loss rate $\langle \dot{M}_S \rangle$ and the system age t_* (Table 2), yielding the exomoon's evaporation fraction $\langle f_{\text{loss}} \rangle \sim t_*/t_{\text{evap}}$. Potentially disintegrated debris systems are flagged as \odot from our mass-loss model, whereas \bigcirc indicates that the tidally heated $T_0 > 2000$ K may imply catastrophic disintegration (Perez-Becker & Chiang 2013). Following analysis, the top exomoon systems are in bold.

The LOS column against the stellar disk is then simply $N_{\text{lo}} \sim \frac{\mathcal{N}}{\pi R_*^2}$. The average LOS column densities we estimate in Table 5 can exceed both Jupiter’s atmospheric column density $\sim 7 \times 10^{11} \text{ cm}^{-2}$ and Jupiter’s $\sim 1000 R_J$ exospheric column $\sim 2.5 \times 10^{10} \text{ cm}^{-2}$ (Section 3.1) by 3 orders of magnitude.

This range of predicted exo-Io column densities can be directly compared to the minimum required column density derived from the observed equivalent widths from high-resolution transmission spectra observations, which we will now describe.

4.3. Sodium and Potassium Gas Column Densities: Constraints from Observations

Despite considerable advances in instrumentation and advanced techniques to probe exoplanet atmospheres with line profiles, the geometrical distribution of the Na I and K I seen in transit cannot be inferred. Given that Na I and K I line cores are capable of probing extremely tenuous pressures, the optically thin regime can illuminate a minimum LOS column density,

$$\langle N \rangle_{\text{obs}} = \frac{W_{\lambda,i}}{\frac{\pi e^2}{m_e c} f_{ik} \lambda^2} \quad (14)$$

(Draine 2011), where f_{ik} is the oscillator strength for the Na D1 and D2 lines and the equivalent width in angstroms $W_{\lambda,i}$. We can now compare this observed column density to our estimates of an exo-Io at a hot Jupiter based on our understanding of alkaline mass loss. The comparison of required column densities indicates that a large majority of the systems are consistent with an exogenic supply of Na I atoms such as an exo-Io. Based on these rough estimates, the supply of exogenic Na I appears to be dominated by atmospheric sputtering (\dot{M}_p) for 10 systems and energy-limited escape (\dot{M}_U) for 3 systems, with only 1 system dominated by escape due to surface heating (\dot{M}_S). The maximum supply, considering all upper limits, is italicized in Table 5. We discuss the limitations and additional plasma interactions in the following section in the context of observing and characterizing these signatures with upcoming instrumentation.

5. Discussion

The activity occurring on close-in irradiated exomoons, as described here, appears to be capable of delivering a significant volatile mass to its host exoplanetary system. The principal question that remains is: how significant is the exogenic mass when compared to the expected endogenic mass, and is this additional mass already detected in the robust transmission spectra observations of Na I and K I? Nominal mass-loss models from hot Jupiters estimate $\sim 10^7 \text{ kg s}^{-1}$ of total mass, corresponding to roughly $\sim 10 \text{ kg s}^{-1}$ of Na for the nominal solar abundance scenarios, whereas our exo-Io model can supply on the order of $4 \times 10^6 \text{ kg s}^{-1}$ of pure Na I, approaching the maximum volcanic output of Io and, in effect, the possible destruction limit of an exo-Io. Section 3 helped qualify the mass of exogenic Na I probed in transmission at a cold Jupiter. For hot Jupiters, more comprehensive searches of volatiles and their spectral imprint with high-resolution echelle spectrographs will certainly improve our understanding of endogenic–exogenic interactions. In the last decade, our early understanding of a hot Jupiter’s environment was limited to H I

and Na I detections at HD 209458b (Charbonneau et al. (2002) and largely described in the seminal paper on atmospheric escape from hot Jupiters (see Murray-Clay et al.’s 2009 Figure 8, summarizing the environment in 1D). Since then, a series of observations may have enhanced our picture.

5.1. A 2D View of Atmospheric Escape: Plasma Tori

In addition to the dozens of alkaline detections, several other extrasolar volatile species, He I (Salz et al. 2018; Spake et al. 2018), Mg I (Vidal-Madjar et al. 2013), and the ions Ca II (Astudillo-Defru & Rojo 2013; Ridden-Harper et al. 2016), Fe II, and Ti II (Hoeijmakers et al. 2018), along with tentative detections of doubly ionized species such as Mg III (Fossati et al. 2010), have been observed, reminiscent of not only Io’s volatiles but also Mercury’s, where the stellar wind interaction is well observed and simulated (e.g., Killen et al. 2001; Leblanc & Johnson 2010; Schmidt 2013a). The magnesium ions were observed in the ultraviolet, where anomalies in the ingress and egress transit spectra at HD 189733b and WASP-12b have already tentatively suggested a plasma torus (Fossati et al. 2010; Ben-Jaffel & Ballester 2014; Kislyakova et al. 2016), as predicted in general by Johnson & Huggins (2006). A plasma torus is a natural consequence when volatiles emanate from an orbiting exogenic source within the magnetosphere of a planet, as the volatiles will eventually be ionized and form a torus of its ejected material. The possibility of a plasma torus adds a second dimension to the hot Jupiter 1D environment described previously, which we illustrate in black in Figure 4. This 2D illustration summarizes the Na I exosphere we describe in this work by our orbital stability constraints and simple modeling of an exo-Io’s Na I escape. We indicate the various scale lengths following the same convention as Murray-Clay et al. (2009), inspired by parameters from HD 209458b, whose escaping atmosphere has been shown to be consistent with the energetic neutral atoms (ENAs) H^* , O^* , and C^{++} (Ben-Jaffel & Sona Hosseini 2010). The dissociative recombination of NaCl^+ , as mentioned in Section 4 yields the ENA Na^* in the form of streams, as shown in Figure 3. A unique consequence of exomoons orbiting hot Jupiters is that they would be directly embedded in the hydrodynamically escaping endogenic medium, rendering the distinction between the two difficult at present. However, with the recent discovery of Na I at a remarkably high altitude, $R_{\text{Na}} \sim 1.5 R_p$, for WASP-49b (Wytenbach et al. 2017), we discuss what may be a strong indication of exogenic sodium, although not unambiguous at present. Further testable predictions, as we have described, include nonsolar Na/K ratios and spectral shifts due to radiation pressure.

5.2. Evidence of Geologically Active Satellites?

5.2.1. Radiation Pressure and Variability Signatures

The radiation pressure on any emitted alkaline atom at hot Jupiters is significant, roughly $\sim 10\times$ that at Mercury, and may lead to an observable spectral shift Δv_{rad} analogous to Mercury’s comet-like Na I and K I tails (Schmidt 2013b; Schmidt et al. 2018). We compute the acceleration due to radiation pressure on an Na I atom following Chamberlain (1961), which can be understood by the commonly used parameter β as the ratio of accelerations due to radiation pressure and gravity. For an orbiting atom, the latter is $\frac{v_{\text{orb}}^2}{a_s}$, so

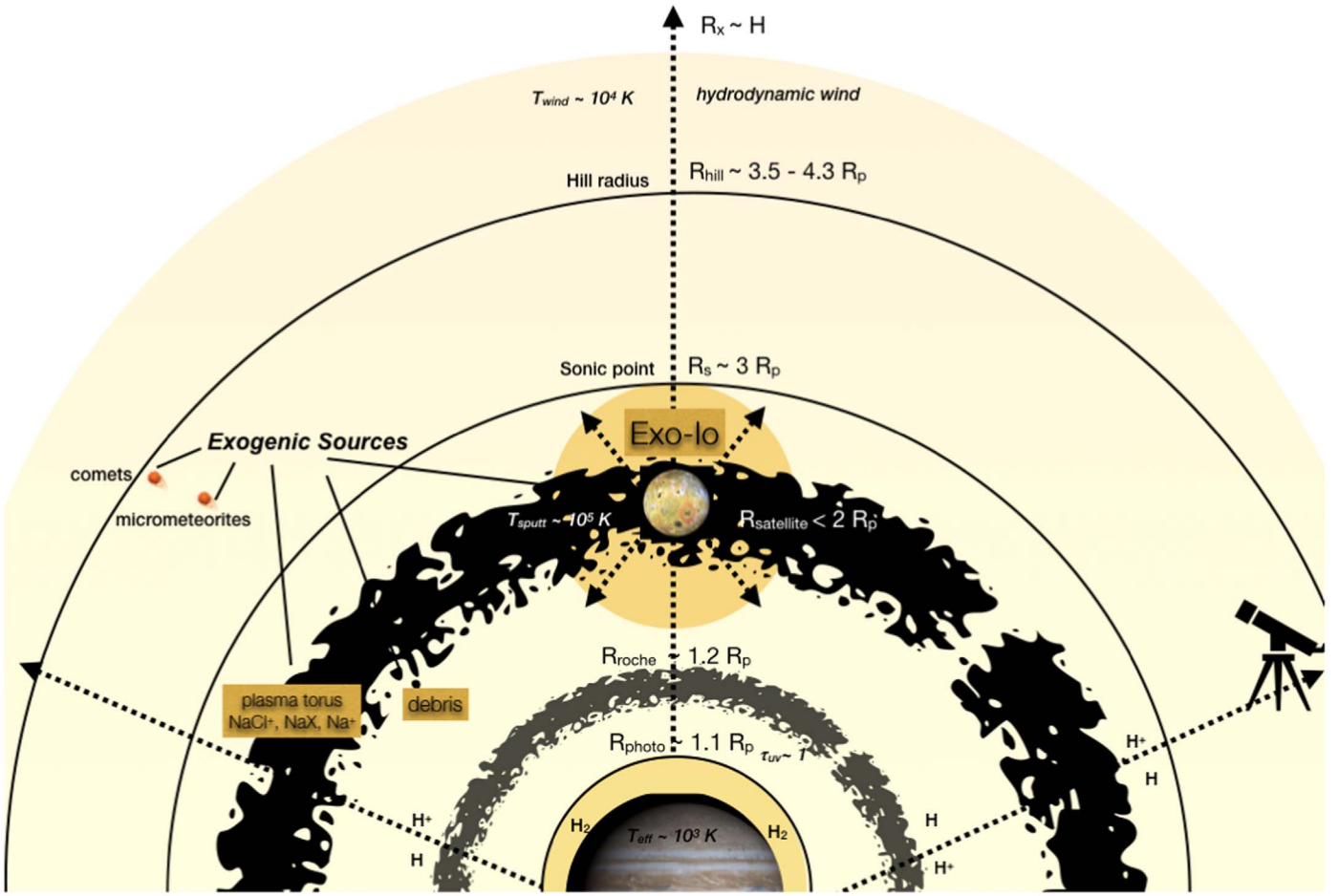


Figure 4. The 2D “birds-eye” architecture of a sodium exosphere at a close-in gas giant exoplanet system. *Endogenic*: an extended sodium layer above the hot Jupiter is shown to illustrate a well-mixed Na I component (yellow). *Exogenic*: an exo-Io sodium cloud (yellow) is shown at $\sim 2 R_p$. Parameters for an escaping atmosphere are overlaid, inspired by the 1D hot Jupiter atmosphere by Murray-Clay et al. (2009). Several other desorbing-exogenic sources (comets, micrometeorites, debris) illustrate the possible endogenic–exogenic interaction contributing to the light yellow exosphere. A full Monte Carlo simulation is likely necessary to describe the precise ion–neutral and electron–neutral interactions in detail, yet a upper atmosphere model by Huang et al. (2017) and high-resolution observations of HD 189733b (Wytenbach et al. 2015) and WASP-49b (Wytenbach et al. 2017) are suggestive of the parameter space. If the hot Jupiter is magnetic, a slowly rotating plasma torus carrying ejected material (in black) should be present. Given that an active satellite would be orbiting close-in at $\sim 20 \text{ km s}^{-1}$ with ejected sodium speeds $\sim 10 \text{ km s}^{-1}$ due to sputtering (i.e., Io), the corresponding kinetic temperature will be on the order of 10^5 K , far hotter than the escaping hydrodynamic wind of the gas giant providing a source for line broadening. The ionized gas H, H⁺ above the photoionization base should also contribute strongly to the plasma density ($n_e \sim 10^9$), possibly resulting in stray sodium spraying throughout the system and into the exosphere.

the parameter can be written as β_s ,

$$\beta_s = \frac{\mathcal{F}_\lambda \frac{\pi e^2 \lambda^2}{m_{\text{Na}} m_e c^3} (f_{\text{D1}} + f_{\text{D2}})}{\frac{v_{\text{orb}}^2}{a_s}}, \quad (15)$$

where \mathcal{F}_λ is the incident stellar radiation flux (Rybicki & Lightman 1979) at the doublet wavelength $\lambda_{\text{NaD1,D2}}$ and $f_{\text{NaD2}} = 0.641$, $f_{\text{NaD1}} = 0.320$ the oscillator strength of the Na D2 and D1 resonance lines, respectively (Draine 2011). In Table 4, we use a blackbody spectrum for an F, G, and K star and estimate β for each exoplanetary system. The values imply blowoff, likely leading to an extended sodium tail of $\sim 10 R_{\text{Io}}$, on average. To appreciate this effect, given that $\sim 50.7 \text{ km s}^{-1}$ corresponds to a shift of 1 \AA , the linear velocity shift on a stagnant Na I cloud due to radiation pressure alone is then $\Delta v_{\text{rad}} \sim a_{\text{rad}} T_{\text{Na}}$, resulting in shifts between 10 and 70 km s^{-1} (~ 0.2 – 1.4 \AA). Of course, if the cloud is vented from an orbiting satellite, the observed shift would be $\pm \gtrsim 20 \text{ km s}^{-1}$, depending on both the movement of the ejected gas and the satellite’s

orbital motion during the observation. Accounting for these additional motions, one may expect Na I and K I clouds to move with respect to the planet’s rest-frame velocity on the $\sim \text{km s}^{-1}$ level. Since a molten exo-Io will additionally thermally evaporate material asymmetrically at the subsolar hemisphere, it is conceivable that spectral shifts due to radiation pressure could be strongly mitigated. Furthermore, at HD 189733b, the leading and trailing limbs ($-5.3^{+1.0}_{-1.4} \text{ km s}^{-1}$ (blueshift) and $+2.23^{+1.3}_{-1.5} \text{ km s}^{-1}$ (redshift), respectively; Loudén & Wheatley 2015) have not been attributed to radiation pressure but rather to eastward equatorial jets, motivated by atmospheric circulation models. On the other hand, HD 209458b (-14.7 km s^{-1}), HAT-P-1b (-3 km s^{-1}), Kelt 20-b (26 km s^{-1}), HD 80606b (-4 km s^{-1}), and possibly the super-Earth 55 Cancri-e (-27 km s^{-1}) also exhibit spectral shifts of Na I and K I (Snellen et al. 2008; Colón et al. 2012; Wilson et al. 2015; Ridden-Harper et al. 2016), suggesting that time-sensitive monitoring of these systems is required. This interaction implies that there would be considerable variability in the Na I and K I

lines, an effect observed for WASP-31b and attributed so far to instrumental effects (Gibson et al. 2019). Ingress and egress observations probing the entirety of the planetary Hill sphere would also help constrain possible variability.

5.2.2. Sodium/Potassium Ratios: Lessons from the Solar System

As Figure 3 depicts, Io’s Na I jets can travel the entirety of Jupiter’s magnetosphere. Therefore, whether Io was the exogenic source of the Na I discovered at Europa (Brown & Hill 1996) was uncertain until the discovery of K I (Brown 2001). As Na/K ratios are suggestive of physical processes, the theoretical Na/K ratio at Europa by Leblanc et al. (2002) and Johnson et al. (2002; see their Table 1), when compared to the observational Na/K ratios at Io and Europa, demonstrated that Europa’s Na I was primarily an endogenic ocean source. As we have no knowledge of the geological composition of the exo-Ios we describe in this work, we can only say with confidence that the ratios should be nonsolar, as tabulated in Table 1. Given that current working models of Na I at hot Jupiters use solar abundances based on the early atomic gas phase predictions for brown dwarfs (Seager & Sasselo 2000; Sudarsky et al. 2000), the observations of Na/K should roughly follow suit, allowing for differences in the volatility and mass of Na and K. The fact that certain alkaline planets have observed K I without a corresponding Na I signature and vice versa at certain alkaline planets is likely problematic for a purely endogenic source. Assuming core accretion or disk instability planet formation mechanisms for the gas giants, the metals should roughly follow solar abundance along the mass-metallicity trend (Mordasini et al. 2012; Thorngren et al. 2016). Despite the differences in mass and alkaline ionization potentials, the Na/K ratios at the three exoplanets with both Na and K are still quite unusual (e.g., $(\text{Na}/\text{K})_{\text{H1b}} \sim 0.5$, along with lunar-like ratios at $(\text{Na}/\text{K})_{\text{XO2b}} \sim 6$ and $(\text{Na}/\text{K})_{\text{W39}} \sim 7$). We encourage follow-up observations of these bodies, especially in K I, which is more difficult to probe than Na I, possibly explaining the nondetections. While no body in the solar system can explain a K I enhancement relative to Na I or the nondetections (Nikolov et al. 2018; retrieval results in $(\text{Na}/\text{K})_{\text{W96}} \gtrsim 10,000$), such a stark contrast could be conceivable geophysically or indicative of an extreme case of mass loss.

5.2.3. An Exo-Io at WASP-49b?

The Na I transit depth was observed at the hot Saturn WASP-49b to extend to $R_{\text{Na}} \sim 1.5 R_p$ (Wytenbach et al. 2017). This anomalously high altitude is roughly $3\times$ higher than HD 189733b, possibly warranting an alternative explanation on the origin of Na I. Furthermore, the line is significantly broader than HD 189733b, suggesting a far more energetic sodium component. Wytenbach et al. (2017) showed with isothermal transmission spectra models that the Na I line wings and core can be fit individually with two distinct temperatures (1400 and 2950 K, respectively). We confirm that the transit depth can be roughly reproduced with an essentially isothermal hydrostatic atmosphere at 2950 K (Figure 5; dotted line). The state-of-the-art 1D hydrodynamic model developed for WASP-49b by Cubillos et al. (2017) suggests, however, that the temperature profile derived based on XUV heating, $\text{Ly}\alpha$ cooling, dissociation, ionization, and recombination is not isothermal. Figure 2 of Cubillos et al. (2017) shows that temperatures near 3000 K only persist between 0.01 and 10 nbar, after which the atmosphere significantly cools. Cubillos et al.’s (2017) Figure 8 attempted to

fit the full line profile with a quasi-hydrodynamic model corresponding to two hydrostatic layers at $T = 1000$ K and an arbitrary isothermal layer at $T = 2950$ K escaping above an assumed Na_2S haze layer at ~ 1 nbar at $100\times$ solar abundance, X_{\odot} . Reproducing this model (Figure 5; blue line), we confirm that it fails to reproduce the transit depth and is far too narrow, as stated by the authors. The endogenic models are problematic due to the large mass of Na I required by the large transit depths. The minimum LOS columns given in Table 5 can easily be converted to total mass integrated over the stellar disk, for which we find a minimum Na I mass of $M_{\text{Na,min}} \gtrsim 10^{6.1} > 1.3 \times 10^6$ kg, or $10\times$ Jupiter’s atmospheric Na I (Section 3.1). Given the above constraint, we can estimate the Na I mass supply assuming a substantial fraction of the absorption is endogenically escaping material. As hot Jupiters’ mass losses are well approximated by energy-limited escape (Equation (9)), an incoming EUV flux of $F_{\text{EUV}} = 2500 \text{ erg s}^{-1} \text{ cm}^{-2}$, and a range of η_{XUV} described above, yields a total gas supply due to mass-loss $\dot{M}_{\text{tot,W49b}} \sim 10^{7.1 \pm 0.3} \text{ kg s}^{-1}$. Assuming the gas is of solar abundance, the Na I supply rate is only $\sim \dot{M}_{\text{Na,W49b}} \sim 10^{1.4 \pm 0.3} \text{ kg s}^{-1}$, corresponding to a bulk Na mass of $M_{\text{Na,escape}} \sim 10^{3.8 \pm 0.3} \text{ kg}$. This implies that the Na I abundance, if endogenically escaping, must be $X_{\text{Na}} \sim 5000 \times X_{\odot}$. A strongly supersolar metallicity is suggested by the calculations of Cubillos et al. (2017), yet such a haze model has difficulty fitting the transit depth. Furthermore, the implied atmospheric metal enrichment would be too large by an order of magnitude (Thorngren & Fortney 2019). It is possible that at such high altitudes, local thermodynamic equilibrium (LTE) breaks down, and a non-LTE distribution could better fit the transit depth, as suspected by recent atmospheric retrieval modeling by Fisher & Heng (2019); however, the precise broadening mechanism is as of yet unidentified.

Using the highest-quality observations of the Na I column abundance in Io’s corona from 1985 to 1997 by Burger et al. (2001), we test the presence of an orbiting exo-Io (Figure 5; red line) based on the parameters in Tables 4 and 5. Assuming the observations can be scaled and then extrapolated inward to the surface, a tidally heated, ionization-limited radial profile of an exo-Io consistent with the power law for Io’s Na I corona would be

$$n_{\text{Exo-Io}}(b) = \eta_T \left(\frac{\tau_{\text{Na,exo-Io}}}{\tau_{\text{Na,Io}}} \right) n_{\text{Io,0}} b^{-3.34} \text{ cm}^{-3}. \quad (16)$$

Here b is the impact parameter in units of R_s , τ is the Na I lifetime ($\tau_{\text{Na,Io}} \sim 4 \text{ hr}$; Wilson et al. 2002), and a tidal efficiency of $\eta_T \sim 10^{5 \pm 0.5}$ is in good agreement with the plasma-driven loss described in Section 4. The column density we estimate in Table 5, $\sim 9 \times 10^{10 \pm 0.4}$, is well within the error of the required column density from observations. The effective kinetic temperature of the gas we set to $\sim 1.4 \times 10^5 \text{ K}$, equivalent to the canonical atmospheric sputtering distribution velocity of $\sim 10 \text{ km s}^{-1}$ (Wilson et al. 2002). We note that the line profile becomes too narrow for a thermal velocity distribution, suggesting a nonthermal velocity distribution venting from an exomoon. If our orbital stability calculation of a critical tidal $Q_{p,W49b} \sim 4 \times 10^9$ for an Io-sized satellite holds against the equilibrium tide limit for hot Jupiters, one might conclude that a geologically active satellite is a natural source for the planetary system’s Na I, as at our Jupiter.

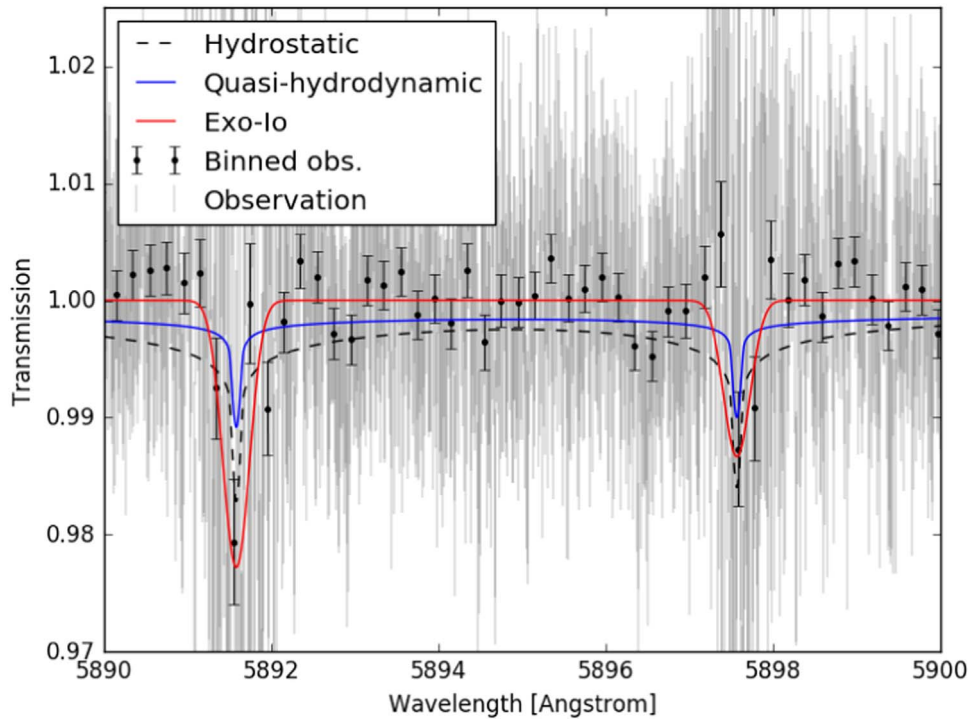


Figure 5. Transmission spectrum of WASP-49b at the Na doublet. We model the endogenic atmosphere with both hydrostatic and quasi-hydrodynamic assumptions. The hydrostatic model (dashed black line) is isothermal at $T \sim 2950$ K, equivalent to the temperature probed by Wyttenbach et al. (2017). The quasi-hydrodynamic atmosphere in blue, as modeled by Cubillos et al. (2017), corresponds to an isothermal planetary wind of $T \sim 3000$ K above a supposed isothermal $T \sim 1000$ K Na_2S haze layer fixed at $\sim 100\times$ solar abundance. We note that like HD 189733b (Huang et al. 2017), an isothermal atmosphere is unlikely. The true nonisothermal hydrodynamic solution would produce an even smaller transit depth due to cooling (Figure 2 of Cubillos et al. 2017). The exogenic source (red line) is identical to the exo-Io of $\eta_T \sim 10^{5\pm0.5}$ we describe in the text, driving a plasma-driven sodium enhancement of $\sim 10^{3.7\pm0.5}\times$ that at Io due to the expected stellar forcing. We employ an escaping sodium density profile (Equation (16)) equivalent to the 1985–1997 observations of Io’s sodium corona (Burger et al. 2001) and ~ 10 km s $^{-1}$ velocity characteristic of atmospheric sputtering. While our energy-limited escape rates also confirm a similar $>100\times$ solar abundance, the planetary wind model cannot reproduce the transit depth (Cubillos et al. 2017). Based on state-of-the-art 1D hydrodynamic modeling, including XUV heating, $\text{Ly}\alpha$ cooling, dissociation, ionization, and recombination by Cubillos et al. (2017), an endogenic atmosphere appears to be unlikely for WASP-49b at present. We therefore find the exo-Io source to be a promising candidate for the sodium line.

6. Conclusions

Given that the prospect of discovering extrasolar satellites with masses $M \lesssim 10^{-2} M_{\oplus}$ by radial velocity or radii $R \lesssim 3 \times 10^{-1} R_{\oplus}$ by transit techniques is bleak at present (Teachey & Kipping 2018; Heller et al. 2019; Kreidberg et al. 2019), we describe in this work how gas signatures of Na I and K I at a hot Jupiter could be indicating the presence of a geologically active satellite subject to the ambient plasma. This appears to be the case for at least one such system, WASP-49b. We use the Jupiter–Io Na I system extending to $\sim 1000 R_J$ as a benchmark for our case study of an exo-Io, remarking on the fact that \sim dozen exoplanetary systems host robust alkaline detections since the initial suggestion of a toroidal exoplanet atmosphere by Johnson & Huggins (2006). We therefore use the well-known orbital parameters of this sample to assess both the survival and possible gas contribution of an exo-Io by modeling the Na I mass loss applicable to the order-of-magnitude level. Working toward a general description of a rocky exomoon orbiting a hot Jupiter, we find several natural consequences.

Foremost, in Section 2 we built on the calculations of massive satellites around tidally locked close-in exoplanets in Cassidy et al. (2009), showing that smaller exo-Ios can, in principle, survive around all observed alkaline systems to date (Figure 1) due to the gravitational forcing of the host star. If an exo-Io were to exist, the canonical condition requires that the critical tidal Q of the planet must suffice, $Q_{p,\text{crit}} < Q_p$, where

the upper limit of Q_p is $\sim 10^{12}$, as found by Goldreich & Nicholson (1977) and improved by Wu (2005a). Based on the nondetection of alkalis around WASP-19b, along with the marginal detections around the ultrashort-period Jupiters WASP-43b, WASP-12b, and WASP-103b, it is conceivable that this upper limit for hot Jupiters is closer to $\sim 10^{11}$. Although the critical orbital period we derive, $\tau_{\text{crit}} \gtrsim 0.5$ days, holds true gravitationally over the lifetime of the planetary system, the thermal destruction of an exo-Io is far more jeopardous based on our mass-loss model of molten irradiated bodies (Section 4.2.3). Catastrophic disintegration due to tidally heated surface temperatures exceeding the ~ 2000 K threshold simulated by Perez-Becker & Chiang (2013) may also suggest a critical exo-Io period beyond ~ 2 days (Figure 1).

Consequently, the Na I at the destroyed systems (Table 5), if confirmed, would then be the volcanic remnants of a disintegrated exomoon, possibly still desorbing in the form of debris depending on the timescales. Survival of an exo-Io should therefore be considered in tandem with its mass loss, as orbital stability dependent on semimajor axis is a necessary yet insufficient condition. Although the stellar proximity and insolation is threatening for the above systems, we find that, for the majority of systems, the stellar tides not only force the exo-Io to remain in orbit but also drive significant tidal heating within the satellite, roughly 5 orders of magnitude higher than Io. This significantly increases the mass flux to the planetary system, possibly contributing to the observed Na I spectra in

transmission at hot Jupiters that could be of endogenic or exogenic origin. While we do not conclude that the rest of the NaI signals are solely exogenic, we cannot rule out this possibility at present. Our case for the exogenic origin of alkalis is made by our solar system's benchmark case of Jupiter's atmospheric transmission spectrum (Section 3) and the ability of Io's magnetospherically driven activity to dominate Jupiter's exospheric NaI emission (Section 4).

Our simple estimates result in an LOS column density of $\sim 7 \times 10^{11}$ Na cm $^{-2}$ for Jupiter's atmosphere. We conclude that the corresponding mass arriving at Jupiter's upper atmosphere, $\dot{M}_{\text{exo}} \sim 5 \times 10^{-5}$ kg s $^{-1}$ (or $\dot{M}_{\text{Na}} \sim 1.2 \times 10^5$ kg integrated over Jupiter), can be sourced exogenically, even in excess of the required amount. In addition to Io's powerful NaI supply of ~ 0.11 kg s $^{-1}$ to Jupiter's atmosphere, the corresponding mass from cosmic dust, $\sim 3.7 \times 10^{-3}$ kg s $^{-1}$, and cometary impacts, ~ 0.13 – 0.9 kg s $^{-1}$, could also supply the NaI based on the decades of monitoring following the 1994 SL9 impact, which we walk through in detail starting in Section 3.1.

To obtain a first estimate on how an exo-Io's NaI supply alone can influence the transmission spectrum of a hot Jupiter, we focus on the range of LOS column densities that easily translate to equivalent widths in Table 3, described in Section 4. Scaling to Io's measured atmospheric sputtering rate of ~ 10 – 100 kg s $^{-1}$ of Na in Equation (7) and acknowledging the fact that an exo-Io orbiting a hot Jupiter would reduce its average NaI lifetime to ~ 10 minutes, resulting in an occulting NaI cloud up to $\sim 1 R_J$, nevertheless yields NaI clouds 3–6 orders of magnitude more dense, on average, than at Io due to the expected close-in irradiation acting on the tidally active body we described. The increases in density, when compared to the minimum observed column densities, are well in agreement and can even be in excess of the required amount, as dictated by the equivalent widths in Table 3. We conclude that several hot Jupiters can be sourced, in principle, by thermally or plasma-driven Na and K loss from an active exo-Io (bold in Table 5).













Several NaI spectra appear to suggest that the NaI is dynamic either redshifted or blueshifted, possibly due to radiation pressure, or broadened, suggesting collisions or a nonthermal NaI distribution. Finally when compared to KI, a few planets have ratios that are largely nonsolar, contrary to endogenic formation theory (e.g., Kreidberg et al. 2014).

This first work on exo-Ios hints at the presence of hidden geologically active satellites in several candidate systems at present, where we suggest that for one such system, WASP-49b, an exo-Io may be the leading explanation. That is, to date, endogenic models cannot reproduce the extraordinarily high altitude of the observed Na, even with parameters from a state-of-the-art hydrodynamically escaping atmosphere. The parameters we derive for our candidate exo-Io orbiting WASP-49b are consistent with our predictions in Tables 4 and 5, and the number density profile and corresponding velocity of NaI we fit is identical to the precise 1985–1997 observations of Io's NaI corona.

As the physical processes we describe in this work are capable of expanding material to the edge of the magnetosphere and/or the Hill sphere of a gas giant system, it is important in this coming decade to start considering exoplanets as exoplanetary systems. The boon of the bright NaI and KI lines may be providing astronomers the first inferences of activity from the remnants of small bodies.

We thank the anonymous referee for helpful comments and suggestions, in particular, motivating an extensive alkaline metal mass-loss model from an irradiated rocky exomoon. The authors thank Phil Arras for guidance and discussion on eddy diffusion and tidal dissipation theory at hot Jupiters. A.V.O. and E.L. thank Kevin Heng for insightful discussions on the normalization degeneracy and NaI resonance line theory. We are also greatly appreciative of Jupiter's transmission spectrum provided by Manuel Lopez-Puertas. A.V.O. expresses gratitude to Pierre Auclair-Desrotour, Wade Henning, Adrien Leleu, and Sebastien Charnoz for insight on dynamic stability and discussions on tidal Q. A.V.O. also thanks Mike Skrutskie for instrumental insight on Na and K variability. R.E.J. acknowledges grant support from the NASA PDS program. C.H. is supported in part by NASA under grant program NNX16AK08G and thanks J. Steffen. B.-O.D. acknowledges support from the Swiss National Science Foundation (SNSF) under grant PP00P2_163967. A.V.O. and C.M. acknowledge support from the SNSF under grant BSSGI0_155816 “Planet-sInTime.” Parts of this work have been carried out within the frame of the National Center for Competence in Research PlanetS supported by the SNSF.

ORCID iDs

Apurva V. Oza  <https://orcid.org/0000-0002-1655-0715>
 Robert E. Johnson  <https://orcid.org/0000-0001-7798-5918>
 Emmanuel Lellouch  <https://orcid.org/0000-0001-7168-1577>
 Carl Schmidt  <https://orcid.org/0000-0002-6917-3458>
 Nick Schneider  <https://orcid.org/0000-0001-6720-5519>
 Chenliang Huang  <https://orcid.org/0000-0001-9446-6853>
 Diana Gamborino  <https://orcid.org/0000-0002-7019-6286>
 Andrea Gebek  <https://orcid.org/0000-0002-0206-8231>
 Aurelien Wyttenbach  <https://orcid.org/0000-0001-9003-7699>
 Brice-Olivier Demory  <https://orcid.org/0000-0002-9355-5165>
 Christoph Mordasini  <https://orcid.org/0000-0002-1013-2811>
 David Dubois  <https://orcid.org/0000-0003-2769-2089>

References

- Agol, E., Steffen, J., Sari, R., & Clarkson, W. 2005, *MNRAS*, **359**, 567
- Alexoudi, X., Mallonn, M., von Essen, C., et al. 2018, *A&A*, **620**, A142
- Asplund, M., Grevesse, N., Sauval, A. J., et al. 2009, *ARA&A*, **47**, 481
- Astudillo-Defru, N., & Rojo, P. 2013, *A&A*, **557**, A56
- Barnes, J. W., & O'Brien, D. P. 2002, *ApJ*, **575**, 1087
- Barstow, J. K., Aigrain, S., Irwin, P. G. J., et al. 2017, *ApJ*, **834**, 50
- Ben-Jaffel, L., & Ballester, G. E. 2014, *ApJL*, **785**, L30
- Ben-Jaffel, L., & Sona Hosseini, S. 2010, *ApJ*, **709**, 1284
- Bézar, B., Lellouch, E., Strobel, D., Maillard, J.-P., & Drossart, P. 2002, *Icar*, **159**, 95
- Bower, D. J., Kitzmann, D., Wolf, A. S., et al. 2019, *A&A*, in press (arXiv:1904.08300)
- Boyajian, T. S., LaCourse, D. M., Rappaport, S. A., et al. 2016, *MNRAS*, **457**, 3988
- Brown, M. E. 2001, *Icar*, **151**, 190
- Brown, M. E., & Hill, R. E. 1996, *Natur*, **380**, 229
- Brown, R. A. 1974, in IAU Symp. 65, Exploration of the Planetary System, ed. A. Woszczyk & C. Iwaniszewska (Dordrecht: Reidel), 527
- Brown, R. A., & Chaffee, F. H., Jr. 1974, *ApJL*, **187**, L125
- Burger, M. H., Schneider, N. M., de Pater, I., et al. 2001, *ApJ*, **563**, 1063
- Burns, J. A., Showalter, M. R., Hamilton, D. P., et al. 1999, *Sci*, **284**, 1146
- Casasayas-Barris, N., Palle, E., Nowak, G., et al. 2017, *A&A*, **608**, A135
- Cassidy, T. A., Mendez, R., Arras, P., Johnson, R. E., & Skrutskie, M. F. 2009, *ApJ*, **704**, 1341

- Chamberlain, J. W. 1961, *Physics of the Aurora and Airglow* (New York: Academic Press)
- Chandrasekhar, S. 1969, *Ellipsoidal Figures of Equilibrium* (New Haven, CT: Yale University Press)
- Charbonneau, D., Brown, T. M., Noyes, R. W., & Gilliland, R. L. 2002, *ApJ*, **568**, 377
- Chen, G., Palle, E., Nortmann, L., et al. 2017, *A&A*, **600**, 11
- Christensen, U. R., Holzwarth, V., & Reiners, A. 2009, *Natur*, **457**, 167
- Colón, K. D., Ford, E. B., Redfield, S., et al. 2012, *MNRAS*, **419**, 2233
- Crovisier, J. 1996, in *IAU Coll. 156, The Collision of Comet Shoemaker–Levy 9 and Jupiter*, ed. K. S. Noll, H. A. Weaver, & P. D. Feldman (Cambridge: Cambridge Univ. Press), 31
- Cubillos, P. E., Fossati, L., Erkaev, N. V., et al. 2017, *ApJ*, **849**, 145
- de Kleer, K., & de Pater, I. 2016, *Icar*, **280**, 378
- de Pater, I., de Kleer, K., Davies, A. G., & Ádámkovics, M. 2017, *Icar*, **297**, 265
- Domingos, R. C., Winter, O. C., & Yokoyama, T. 2006, *MNRAS*, **373**, 1227
- Draine, B. T. 2011, *Physics of the Interstellar and Intergalactic Medium* (Princeton, NJ: Princeton Univ. Press)
- Fegley, B., & Cameron, A. G. W. 1987, *E&PSL*, **82**, 207
- Fegley, B., & Zolotov, M. Y. 2000, *Icar*, **148**, 193
- Fischer, P. D., Knutson, H. A., Sing, D. K., et al. 2016, *ApJ*, **827**, 19
- Fisher, C., & Heng, K. 2019, *ApJ*, **881**, 25
- Fossati, L., Haswell, C. A., Froning, C. S., et al. 2010, *ApJL*, **714**, L222
- Fuller, M., Molaro, P., Buzzi, L., & Valisa, P. 2013, *ApJL*, **771**, L21
- Fulton, B. J., & Petigura, E. A. 2018, *AJ*, **156**, 264
- Gardner, C. S., Liu, A. Z., Marsh, D. R., Feng, W., & Plane, J. M. C. 2014, *JGRA*, **119**, 7870
- Gibson, N. P., de Mooij, E. J. W., Evans, T. M., et al. 2019, *MNRAS*, **482**, 606
- Goldreich, P., & Nicholson, P. D. 1977, *Icar*, **30**, 301
- Griessmeier, J.-M., Zarka, P., & Spreeuw, H. 2007, *A&A*, **475**, 359
- Haff, P. K., Watson, C. C., & Yung, Y. L. 1981, *JGR*, **86**, 6933
- Hanson, W. B., & Donaldson, J. S. 1967, *JGR*, **72**, 5513
- Heller, R., Rodenbeck, K., & Bruno, G. 2019, *A&A*, **624**, A95
- Heng, K. 2016, *ApJL*, **826**, L16
- Heng, K., Wytenbach, A., Lavie, B., et al. 2015, *ApJL*, **803**, L9
- Hoeijmakers, H. J., Ehrenreich, D., Heng, K., et al. 2018, *Natur*, **560**, 453
- Huang, C., Arras, P., Christie, D., & Li, Z.-Y. 2017, *ApJ*, **851**, 150
- Huebner, W. F., & Mukherjee, J. 2015, *P&SS*, **106**, 11
- Huitson, C. M., Sing, D. K., Vidal-Madjar, A., et al. 2012, *MNRAS*, **422**, 2477
- Hunten, D. M. 1967, *SSRv*, **6**, 493
- Hunten, D. M., & Wallace, L. 1967, *JGR*, **72**, 69
- Ingersoll, A. P. 1989, *Icar*, **81**, 298
- Jin, S., & Mordasini, C. 2018, *ApJ*, **853**, 163
- Jin, S., Mordasini, C., Parmentier, V., et al. 2014, *ApJ*, **795**, 65
- Johnson, R. E. 1990, *Energetic Charged-Particle Interactions with Atmospheres and Surfaces* (Berlin: Springer), 84
- Johnson, R. E. 2004, *ApJL*, **609**, L99
- Johnson, R. E., & Huggins, P. J. 2006, *PASP*, **118**, 1136
- Johnson, R. E., Leblanc, F., Yakshinskiy, B. V., & Madey, T. E. 2002, *Icar*, **156**, 136
- Johnson, R. E., Luhmann, J. G., Tokar, R. L., et al. 2006a, *Icar*, **180**, 393
- Johnson, R. E., Oza, A., Young, L. A., Volkov, A. N., & Schmidt, C. 2015, *ApJ*, **809**, 43
- Johnson, R. E., Smith, H. T., Tucker, O. J., et al. 2006b, *ApJL*, **644**, L137
- Johnson, R. E., Volkov, A. N., & Erwin, J. T. 2013, *ApJL*, **768**, L4
- Kao, M. M., Hallinan, G., Pineda, J. S., Stevenson, D., & Burgasser, A. 2018, *ApJS*, **237**, 25
- Khalafinejad, S., Salz, M., Cubillos, P. E., et al. 2018, *ApJ*, **618**, A98
- Khalafinejad, S., von Essen, C., Hoeijmakers, H. J., et al. 2017, *A&A*, **598**, A131
- Killen, R. M., Potter, A. E., Reiff, P., et al. 2001, *JGR*, **106**, 20509
- Kipping, D. M. 2009, *MNRAS*, **392**, 181
- Kislyakova, K. G., Holmström, M., Lammer, H., Odert, P., & Khodachenko, M. L. 2014, *Sci*, **346**, 981
- Kislyakova, K. G., Pilat-Lohinger, E., Funk, B., et al. 2016, *MNRAS*, **461**, 988
- Kreidberg, L., Bean, J. L., Désert, J.-M., et al. 2014, *ApJL*, **793**, L27
- Kreidberg, L., Luger, R., & Bedell, M. 2019, *ApJL*, **877**, L15
- Küppers, M., & Schneider, N. M. 2000, *GeoRL*, **27**, 513
- Lainey, V., & Tobie, G. 2005, *Icar*, **179**, 485
- Lammer, H., Odert, P., Leitzinger, M., et al. 2009, *A&A*, **506**, 399
- Langland-Shula, L. E., Vogt, S. S., Charbonneau, D., Butler, P., & Marcy, G. 2009, *ApJ*, **696**, 1355
- Leblanc, F., Doressoundiram, A., Schneider, N., et al. 2008, *GeoRL*, **35**, L18204
- Leblanc, F., & Johnson, R. E. 2010, *Icar*, **209**, 280
- Leblanc, F., Johnson, R. E., & Brown, M. E. 2002, *Icar*, **159**, 132
- Leblanc, F., Potter, A. E., Killen, R. M., & Johnson, R. E. 2005, *Icar*, **178**, 367
- Lellouch, E. 1996, in *IAU Coll. 156, The Collision of Comet Shoemaker–Levy 9 and Jupiter*, ed. K. S. Noll, H. A. Weaver, & P. D. Feldman (Cambridge: Cambridge Univ. Press), 213
- Lellouch, E., Ali-Dib, M., Jessup, K.-L., et al. 2015, *Icar*, **253**, 99
- Lellouch, E., Belton, M., de Pater, I., et al. 1992, *Icar*, **98**, 271
- Lellouch, E., Belton, M., de Pater, I., Gulkis, S., & Encenaz, T. 1990, *Natur*, **346**, 639
- Lellouch, E., Bézard, B., Moreno, R., et al. 1997, *P&SS*, **45**, 1203
- Lellouch, E., Bézard, B., Moses, J. I., et al. 2002, *Icar*, **159**, 112
- Lellouch, E., Paubert, G., Moses, J. I., Schneider, N. M., & Strobel, D. F. 2003, *Natur*, **421**, 45
- Lellouch, E., Strobel, D. F., Belton, M. J. S., et al. 1996, *ApJL*, **459**, L107
- Lide, D. R. 1994, *CRC Handbook of Chemistry and Physics. A Ready-reference Book of Chemical and Physical Data* (Boca Raton, FL: CRC Press)
- Lodders, K. 2010, *ASSP*, **16**, 379
- Louden, T., & Wheatley, P. J. 2015, *ApJL*, **814**, L24
- Marchis, F., Le Mignant, D., Chaffee, F. H., et al. 2005, *Icar*, **176**, 96
- Matsakos, T., Uribe, A., & Königl, A. 2015, *A&A*, **578**, A6
- McDonnell, W. J., Goldstein, D. B., Varghese, P. L., & Trafton, L. M. 2017, *Icar*, **294**, 81
- Mendillo, M., Baumgardner, J., Flynn, B., & Hughes, W. J. 1990, *Natur*, **348**, 312
- Montañés-Rodríguez, P., González-Merino, B., Pallé, E., López-Puertas, M., & García-Melendo, E. 2015, *ApJL*, **801**, L8
- Morabito, L. A., Synnott, S. P., Kupferman, P. N., & Collins, S. A. 1979, *Sci*, **204**, 972
- Mordasini, C., Alibert, Y., Benz, W., Klahr, H., & Henning, T. 2012, *A&A*, **541**, A97
- Moreno, R., Marten, A., Matthews, H. E., & Biraud, Y. 2003, *P&SS*, **51**, 591
- Moses, J. I., & Poppe, A. R. 2017, *Icar*, **297**, 33
- Moulet, A., Lellouch, E., Gurwell, M., et al. 2015, *AAS/DPS Meeting*, **47**, 311.31
- Moulet, A., Lellouch, E., Moreno, R., et al. 2013, *ApJ*, **776**, 32
- Murray-Clay, R. A., Chiang, E. I., & Murray, N. 2009, *ApJ*, **693**, 23
- Nikolov, N., Sing, D. K., Fortney, J. J., et al. 2018, *Natur*, **557**, 526
- Nikolov, N., Sing, D. K., Gibson, N. P., et al. 2016, *ApJ*, **832**, 191
- Nikolov, N., Sing, D. K., Pont, F., et al. 2014, *MNRAS*, **437**, 46
- Noack, L., Rivoldini, A., & Van Hoolst, T. 2017, *PEPI*, **269**, 40
- Noll, K. S., Geballe, T. R., & Knacke, R. F. 1995, *ApJL*, **453**, L49
- Ogilvie, G. I. 2014, *ARA&A*, **52**, 171
- Ogilvie, G. I., & Lin, D. N. C. 2004, *ApJ*, **610**, 477
- Ogilvie, G. I., & Lin, D. N. C. 2007, *ApJ*, **661**, 1180
- Pallé, E., Zapatero Osorio, M. R., Barrena, R., Montañés-Rodríguez, P., & Martín, E. L. 2009, *Natur*, **459**, 814
- Parker, E. N. 1964, *ApJ*, **139**, 72
- Passy, J.-C., Mac Low, M.-M., & De Marco, O. 2012, *ApJL*, **759**, L30
- Peale, S. J., Cassen, P., & Reynolds, R. T. 1979, *Sci*, **203**, 892
- Perez-Becker, D., & Chiang, E. 2013, *MNRAS*, **433**, 2294
- Poppe, A. R. 2016, *Icar*, **264**, 369
- Postberg, F., Kempf, S., Schmidt, J., et al. 2009, *Natur*, **459**, 1098
- Potter, A., & Morgan, T. 1985, *Sci*, **229**, 651
- Potter, A. E., & Morgan, T. H. 1986, *Icar*, **67**, 336
- Potter, A. E., & Morgan, T. H. 1988, *Sci*, **241**, 675
- Punzi, K. M., Kastner, J. H., Melis, C., et al. 2018, *AJ*, **155**, 33
- Rappaport, S., Levine, A., Chiang, E., et al. 2012, *ApJ*, **752**, 1
- Ridden-Harper, A. R., Snellen, I. A. G., Keller, C. U., et al. 2016, *A&A*, **593**, A129
- Rogers, T. M. 2017, *NatAs*, **1**, 0131
- Rybicki, G. B., & Lightman, A. P. 1979, *Radiative Processes in Astrophysics* (New York: Wiley-Interscience)
- Salz, M., Czesla, S., Schneider, P. C., et al. 2018, *A&A*, **620**, A97
- Schmidt, C. 2016, *Icar*, **265**, 35
- Schmidt, C., Johnson, R. E., Mendillo, M., et al. 2015a, *AGUFM*, **SM31B**
- Schmidt, C., Reardon, K., Killen, R. M., et al. 2016, *AGUFM*, **P53B**
- Schmidt, C. A. 2013a, PhD thesis, Boston Univ.
- Schmidt, C. A. 2013b, *JGRA*, **118**, 4564
- Schmidt, C. A., Johnson, R. E., Baumgardner, J., & Mendillo, M. 2015b, *Icar*, **247**, 313
- Schmidt, C. A., Leblanc, F., Reardon, K., et al. 2018, *LPICo*, **2047**, 6022
- Schneider, N., & Trauger, J. 1995, *ApJ*, **450**, 450
- Schneider, N. M., Burger, M. H., Schaller, E. L., et al. 2009, *Natur*, **459**, 1102
- Schneider, N. M., Hunten, D. M., Wells, W. K., Schultz, A. B., & Fink, U. 1991, *ApJ*, **368**, 298

- Seager, S., & Sasselov, D. D. 2000, [ApJ](#), **537**, 916
- Seidel, J. V., Ehrenreich, D., Wytenbach, A., et al. 2019, arXiv:1902.00001
- Sing, D. K., Désert, J.-M., Fortney, J. J., et al. 2011, [A&A](#), **527**, A73
- Sing, D. K., Fortney, J. J., Nikolov, N., et al. 2016, [Natur](#), **534**, 529
- Sing, D. K., Huitson, C. M., Lopez-Morales, M., et al. 2012, [MNRAS](#), **426**, 1663
- Sing, D. K., Wakeford, H. R., Showman, A. P., et al. 2015, [MNRAS](#), **446**, 2428
- Skrutskie, M. F., de Kleer, K. R., Stone, J., et al. 2017, AAS/DPS Meeting, **49**, 407.02
- Slipher, V. M. 1929, PA, **37**, 327
- Snellen, I. A. G., Albrecht, S., de Mooij, E. J. W., & Le Poole, R. S. 2008, [A&A](#), **487**, 357
- Spake, J. J., Sing, D. K., Evans, T. M., et al. 2018, [Natur](#), **557**, 68
- Spencer, J. R., Rathbun, J. A., Travis, L. D., et al. 2000, [Sci](#), **288**, 1198
- Spencer, J. R., Stern, S. A., Cheng, A. F., et al. 2007, [Sci](#), **318**, 240
- Sprague, A. L., Kozłowski, R. W. H., Hunten, D. M., et al. 1997, [Icar](#), **129**, 506
- Sudarsky, D., Burrows, A., & Pinto, P. 2000, [ApJ](#), **538**, 885
- Sullivan, H. M., & Hunten, D. M. 1962, [Natur](#), **195**, 589
- Sullivan, H. M., & Hunten, D. M. 1964, [CaJPh](#), **42**, 937
- Szalay, J. R., Horányi, M., Colaprete, A., & Sarantos, M. 2016, [GeoRL](#), **43**, 6096
- Teachey, A., & Kipping, D. M. 2018, [SciA](#), **4**, eaav1784
- Thomas, N. 1996, [A&A](#), **313**, 306
- Thomas, N., Bagenal, F., Hill, T. W., & Wilson, J. K. 2004, in *The Io Neutral Clouds and Plasma Torus*, ed. F. Bagenal, T. E. Dowling, & W. B. McKinnon (Cambridge: Cambridge Univ. Press), 561
- Thorngren, D., & Fortney, J. J. 2019, [ApJL](#), **874**, L31
- Thorngren, D. P., Fortney, J. J., Murray-Clay, R. A., & Lopez, E. D. 2016, [ApJ](#), **831**, 64
- Trafton, L. 1975, [Natur](#), **258**, 690
- Tsang, C. C. C., Spencer, J. R., Lellouch, E., et al. 2013, [Icar](#), **226**, 1177
- Tsang, C. C. C., Spencer, J. R., Lellouch, E., Lopez-Valverde, M. A., & Richter, M. J. 2016, [JGRE](#), **121**, 1400
- Valek, P., McComas, D., Kurth, W., et al. 2018, in 42nd COSPAR Scientific Assembly, **B5.1-3-18**
- van Lieshout, R., Min, M., & Dominik, C. 2014, [A&A](#), **572**, A76
- Vanderburg, A., Johnson, J. A., Rappaport, S., et al. 2015, [Natur](#), **526**, 546
- Vidal-Madjar, A., Huitson, C. M., Bourrier, V., et al. 2013, [A&A](#), **560**, A54
- Vidal-Madjar, A., Sing, D. K., Lecavelier Des Etangs, A., et al. 2011, [A&A](#), **527**, A110
- Volkov, A. N., & Johnson, R. E. 2013, [ApJ](#), **765**, 90
- Volkov, A. N., Johnson, R. E., Tucker, O. J., & Erwin, J. T. 2011, [ApJL](#), **729**, L24
- Watson, A. J., Donahue, T. M., & Walker, J. C. G. 1981, [Icar](#), **48**, 150
- Weidner, C., & Horne, K. 2010, [A&A](#), **521**, A76
- Wilson, J. K., Mendillo, M., Baumgardner, J., et al. 2002, [Icar](#), **157**, 476
- Wilson, J. K., Mendillo, M., & Spence, H. E. 2006, [JGRA](#), **111**, A07207
- Wilson, P. A., Sing, D. K., Nikolov, N., et al. 2015, [MNRAS](#), **450**, 192
- Wong, M. C., & Johnson, R. E. 1996a, [JGR](#), **101**, 23243
- Wong, M. C., & Johnson, R. E. 1996b, [JGR](#), **101**, 23255
- Wu, Y. 2005a, [ApJ](#), **635**, 674
- Wu, Y. 2005b, [ApJ](#), **635**, 688
- Wytenbach, A., Ehrenreich, D., Lovis, C., Udry, S., & Pepe, F. 2015, [A&A](#), **577**, A62
- Wytenbach, A., Lovis, C., Ehrenreich, D., et al. 2017, [A&A](#), **602**, A36
- Zuluaga, J. I., Kipping, D. M., Sucerquia, M., & Alvarado, J. A. 2015, [ApJL](#), **803**, L14